CHEMISTRY OF MATERIALS

Open Access

This article is licensed under CC-BY-NC-ND 4.0

pubs.acs.org/cm

Review

Recent Advances in the Application of Magnetite (Fe_3O_4) in Lithium-Ion Batteries: Synthesis, Electrochemical Performance, and Characterization Techniques

Published as part of Chemistry of Materials special issue "In Memory of Prof. Francis DiSalvo".

Haoze Ren, Han Li, Patrick Barry, Zhongling Wang, Armando Rodriguez Campos, Esther S. Takeuchi, Amy C. Marschilok, Shan Yan, Kenneth J. Takeuchi, and Elsa Reichmanis*

Cite This: *Chem. Mater.* 2024, 36, 9299−9319

Read Online

ACCESS | Metrics & More | Article Recommendations

ABSTRACT: With the promotion of portable energy storage devices and the popularization of electric vehicles, lithium-ion battery (LiB) technology plays a crucial role in modern energy storage systems. Over the past decade, the demands for LiBs have centered around high energy density and long cycle life. These parameters are often determined by the characteristics of the active materials in the electrodes. Given its high abundance, environmental friendliness, low cost and high capacity, magnetite (Fe_3O_4) emerges as a promising anode material. However, the practical application of Fe_3O_4 faces challenges, such as significant volume expansion during cycling. To overcome these obstacles and facilitate the commercialization of Fe_3O_4, a comprehensive understanding of its properties and behavior is essential. This review provides an overview of recent Fe_3O_4 research advances, focusing on its synthesis, factors influencing its electrochemical performance, and characterization techniques. By thoroughly understanding the characteristics of Fe_3O_4 in LiB applications, we can optimize its properties and enhance its performance, thereby paving the way for its widespread use in energy storage applications. Additionally, the review concludes with perspectives on promoting the commercialization of Fe_3O_4 in LiBs and future research directions.

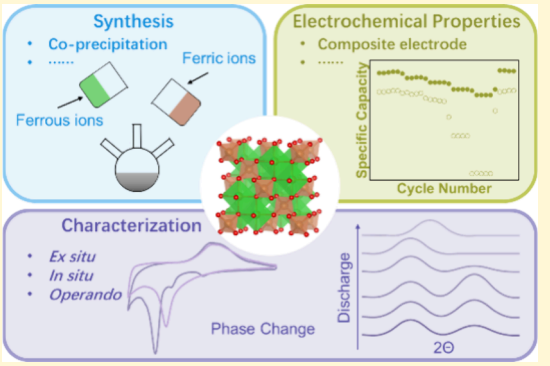

INTRODUCTION

The development of energy technologies is a cornerstone of human progress and has shaped societies and economies throughout history.[1,2] As the world progresses through the 21st century, the urgent need for sustainable and renewable energy has become more apparent.[3] Climate change, environmental degradation, and the finiteness of fossil fuels have driven the global push toward cleaner and more efficient energy solutions.[4] Renewable energy sources such as solar, wind, hydro and geothermal have made great strides, promising to reduce our carbon footprint and reliance on nonrenewable resources.[5] Solar panels and wind turbines are now ubiquitous, reflecting society's broader commitment to sustainable development. Despite these advances, integrating renewable energy into existing power grids still faces challenges in storage, reliability, and scalability.[6] This is where the development of advanced energy storage systems, especially batteries, comes in.[7] Effective energy storage solutions are essential to balancing supply and demand, and ensuring a stable and reliable supply of electricity.[8]

Among the various battery technologies, lithium-ion batteries (LiBs) have emerged as a dominant force due to their high energy density, long cycle life, and decreasing costs.[9] Since the commercialization of LiBs in 1991, the market demand for these batteries has been steadily increasing.[10] For years, lithium cobalt oxide (LCO, 140 mAh g^{-1}) has been the predominant cathode material, while graphite (372 mAh g^{-1}) has been widely used as the anode material.[11] However, the relatively low theoretical capacities of both have posed significant obstacles to advancing the state-of-the-art in LiB technology.[12] Particularly in high-demand sectors such as transportation and grid storage, the volume/weight capacity and production cost of LiBs remain major challenges.[13] Therefore, the pursuit of higher capacity and more cost-effective materials is crucial for ushering in the next LiB generation. In the electric vehicle sector alone, target energy densities should exceed 750 Wh L^{-1} and 350 Wh kg^{-1}.[14] To

Received: July 18, 2024
Revised: September 3, 2024
Accepted: September 5, 2024
Published: September 18, 2024

© 2024 The Authors. Published by American Chemical Society

achieve this goal, in recent years, various novel electrode active materials have garnered increasing attention. Examples include lithium iron phosphate (LFP),[15] and lithium nickel manganese cobalt oxide (NMC)[16] as a cathode active material, and nickel oxide (NiO),[17] manganese oxide (MnO),[18] silicon (Si),[19] and magnetite (Fe_3O_4)[20] as options for the anode. Among these, LFP has gradually become commercialized, with a significant portion of the current LiB market employing it as the cathode material.

LFP, like graphite and many of the cathode materials listed above, is an insertion-type material.[21−23] However, in the pursuit of high-capacity anode materials for next-generation LiBs, conversion-type transition-metal-based compounds present an opportunity for higher theoretical capacity.[24,25] Recent progress in the development of these materials is highlighted by nanoengineering, integration of low-dimensional nanostructures, porous architectures, hollow configurations, and integration with carbon materials. The approaches aim to improve the cycling and stability performance of the anode materials, addressing challenges such as low conductivity and the detrimental effects of conversion-induced pulverization.[26] Advancements in transition metal oxide-based conversion technology hold promise for higher specific capacity, enhanced rate capability, and prolonged cycle life.

Conversion-type electrode materials, noted for their cost-effectiveness and natural abundance have substantial barriers to practical implementation.[27,28] Low conductivity in conversion materials and electrolyte involvement to passivate surfaces hinder full utilization and functional cell electrochemistry.[29] Conversion reactions are associated with phase and volume changes often accompanied by thick solid electrolyte interphase films, reducing electrode cyclability.[30] Additionally, high voltage hysteresis decreases charge/discharge efficiency and can cause battery heating during operation.

Among all the anode material options, Fe_3O_4, a conversion-type anode material (CTAM), stands out as an exceptional material with multiple valence states (Fe^0, Fe^{2+} and Fe^{3+}) to provide diverse redox pairs.[31] Magnetite displays a high theoretical capacity (~920 mAh g^{-1}) and undergoes relatively low, but still significant, volume expansion (~200%).[32] Furthermore, Fe_3O_4 possesses abundant lithium-ion (Li^+) storage sites and a multiphase reaction mechanism, including chemical reactions between metallic iron and oxide, which can enhance Li^+ storage capacity and improve battery performance.[33] From a commercial perspective, iron is the most abundant element on Earth (about 80% by mass) making its sourcing environmentally friendly, inexpensive and nontoxic, and it can be synthesized through simple and safe techniques.[34−36] As early as the 1980s, Thackeray, Coetzer, and Goodenough discovered that lithium could be inserted into the Fe_3O_4 lattice, exhibiting an impressive specific capacity of up to 924 mAh g^{-1}. However, with the increasing demand for high-capacity, high-stability LiBs, Fe_3O_4 still has several issues that need to be addressed such as the low electrical conductivity and the significant volume expansion during cycling.[37]

This review focuses on the advancements in the application of Fe_3O_4 in LiBs. These advancements contribute to improving the capacity and cycle life of battery systems, driving the emergence of next-generation energy storage solutions.[38] The discussion begins with the synthesis of Fe_3O_4 nanoparticles, analyzing and comparing the advantages and disadvantages of different synthesis methods.[39] Highlighted are key factors that influence the synthesis stage and further affect Fe_3O_4 battery performance. Controlling crystallite size during the synthesis process is crucial in developing energy storage materials, enhancing electron and ion diffusion within electrodes.[10] Next, we summarize progress in Fe_3O_4-based battery research from three perspectives: nanostructuring,[40] structural design,[41,42] and composite electrodes.[43,44] In brief, nanoscale Fe_3O_4 exhibits better electrochemical performance. The advantages and disadvantages of different structural configurations of Fe_3O_4 particles need to be considered from various aspects, including conductivity, ion transport and electrode stability. For composite electrodes, the variety of composite materials offers multiple avenues for optimizing Fe_3O_4-based batteries.[45−47] Factors such as crystallite size, structure and electrode composition significantly influence electrochemical performance, especially for dense materials like Fe_3O_4, which is a focal point in LiBs due to its high capacity and cost-effectiveness. Following this, the various characterization methods applied in Fe_3O_4 battery research are summarized. These methods leverage the unique characteristics of Fe_3O_4 in battery applications, such as irreversible phase changes, energy loss and changes, and magnetic changes in the electrodes during cycling, to conduct comprehensive and in-depth research on Fe_3O_4 for battery applications. A deeper understanding of Fe_3O_4-based batteries will further promote the improvement of storage systems to meet contemporary and forthcoming energy performance standards.

LATTICE STRUCTURE

An inverse spinel structure features the tetrahedral site (8a) occupied by one of the M^{3+} cations, while the other M^{3+} cation and the M^{2+} cation occupy octahedral sites (16d) within a cubic-close-packed (ccp) O-anion array.[48] Fe_3O_4 crystallizes into this inverse spinel structure, characterized by a ccp arrangement of O^{2-} anions. The formula of magnetite, $Fe^{2+}Fe^{3+}{}_2O_4$, reflects its unit lattice, which contains 8 Fe^{2+} cations and 16 Fe^{3+} cations. These cations are uniformly distributed between the tetrahedral and octahedral sites, with Fe^{3+} ions occupying the tetrahedral (8a) sites, and both Fe^{3+} and Fe^{2+} ions occupying the octahedral (16d) sites (Figure 1).[49] In lithiation, two Li^+ will first insert into the Fe_3O_4 lattice to form $Li_xFe_3O_4$ without undergoing a change in phase. With further lithiation, the structure transitions into a LiO_2·FeO rock-salt phase, and ultimately, continued lithiation results in a LiO_2·Fe nanocomposite phase.

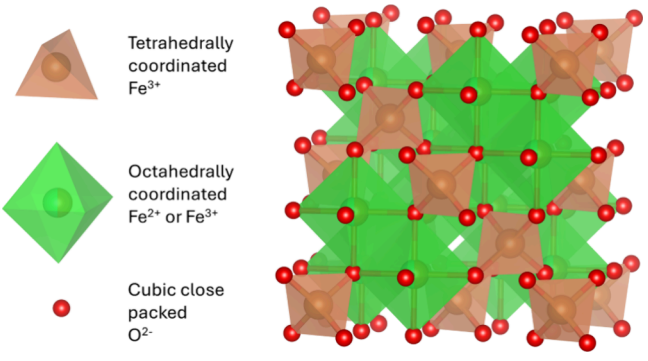

Figure 1. Crystal structure of magnetite.

https://doi.org/10.1021/acs.chemmater.4c02013
Chem. Mater. 2024, 36, 9299−9319

SYNTHESIS

The fabrication of Fe_3O_4 nanoparticles can be achieved through two primary methods: top-down and bottom-up approaches.[50,51] The top-down approach starts with bulk magnetite and employs techniques such as ball milling, sputtering, and aerosol spray pyrolysis to produce nanoparticles.[52−54] Conversely, the bottom-up approach involves forming nanoparticles from molecular precursors that contain iron, under specific experimental conditions.[55,56] Common bottom-up techniques include thermal decomposition, microemulsion, sono-chemical processes, and electrochemical synthesis.[57−59] Notably, coprecipitation is a widely researched and applied method because it involves mixing appropriate metal salts with suitable precipitants under controlled temperature and pH conditions, allowing nanoparticles to coprecipitate from the solution. During this process, variables such as temperature, pH, reaction time, and stirring rate can be adjusted to influence the morphology, size and distribution of the nanoparticles.[60,61] This method is favored for its simplicity, cost-effectiveness, and broad applicability in nanomaterial preparation. This section focuses on bottom-up synthesis methods, discussing the advantages and disadvantages of each (Table 1).

Table 1. Fe_3O_4 Synthesis Methods (Bottom-up) Comparison

method	advantage	disadvantage	ref
Thermal decomposition	Simple operation	Energy-consuming	62−64
	Cost-effective	Potential toxicity	
	Fast production time		
	Characteristics controllable		
Microemulsion	Simple operation	Potential toxicity	65−68
	Well-dispersed production	Industrial scale-up limited	
	Characteristics controllable	Low efficiency	
Sol−gel	Well-dispersed production Low temperature	Time consuming	69,70
	Structure controllable	Potential toxicity	
Electrochemical synthesis	Structure controllable	High cost	71,72
	Characteristics controllable	Complex operation	
	Environmentally friendly	Low efficiency	
	High production purity		
Coprecipitation	Simple operation	Complex post-treatment	73,74
	High efficiency	pH sensitive	
	Low temperature		
	Industrial scale-up		

The thermal decomposition method is a precise technique for synthesizing crystalline Fe_3O_4 nanoparticles.[62] It starts with dissolving suitable iron salts (such as ferric chloride, ferric nitrate, and ferric sulfate) in a solvent to create a solution. This solution is then heated to elevated temperatures (usually between 200 and 300 °C), where the iron salts undergo thermal decomposition to yield oxide precursors. These precursors gradually crystallize into Fe_3O_4 nanoparticles. Throughout this process, parameters such as temperature, reaction time, and stirring rate are controlled to tune the morphology, size, and distribution of the nanoparticles.[63] Subsequent steps include precipitation, washing, and drying to obtain pure magnetite nanoparticles. The method offers several advantages: it is relatively simple, requires minimal experimental equipment and materials, and is cost-effective. Moreover, adjusting reaction conditions such as temperature and reaction time, allows precise control over the nanoparticle characteristics to suit various applications. However, thermal decomposition has limitations. It is energy-intensive, and the decomposition process can be time-consuming and result in low efficiency. Additionally, it requires the use of expensive and hazardous substances like high-boiling-point organic solvents, which can increase production costs and pose environmental and health risks.[64]

Microemulsion is another reduced particle size synthesis method.[65] This process uses microemulsions consisting of minuscule water droplets stabilized by surfactants and uniformly dispersed within an oil phase or organic solvent. These droplets act as microreactors, where the exchange of reactants occurs through the collision of droplets within the microemulsion.[66] The advantage of this technique lies in the restricted reaction space provided by the microdroplets, which aids in controlling the size and morphology of the nanoparticles. Due to the presence of surfactants, the Fe_3O_4 nanoparticles synthesized through this method exhibit remarkably low aggregation.[67] Moreover, by adjusting the composition of the microemulsion, such as the type and concentration of surfactants and the size of the droplets, the characteristics of the nanoparticles can be finely tuned. However, the formation of microemulsions requires significant amounts of surfactants and/or cosurfactants, which at high concentrations can be irritants. Additionally, the industrial-scale production of this technique remains limited.[68]

The sol−gel process is a prevalent method for synthesizing nanomaterials, which involves the transformation of liquid precursors into solid materials.[69] Specifically, precursor materials are uniformly mixed. Subsequent hydrolysis or polycondensation reactions are performed, followed by further aging, which induces the gradual aggregation of colloidal particles, thereby forming a polymer gel with a three-dimensional network structure. Subsequently, various processes such as drying and sintering are applied, ultimately yielding nanomaterials. The sol−gel method allows for the synthesis of various complex materials at relatively low temperatures and provides precise control over the chemical composition and microstructure of materials.[70] However, it typically requires extended reaction times.

The electrochemical synthesis method is predicated on the oxidation of a sacrificial anode at high potentials leading to the dissolution of metal ions into the solution, followed by their reduction at lower potentials to form precipitates, thereby synthesizing nanoparticles.[71] Specifically, a sacrificial iron anode is oxidized under high voltage to release iron ions into the solution, which then react with hydroxide ions (OH^-) produced by the cathodic reduction of water to form ferric hydroxide ($Fe(OH)_3$). In an alkaline environment, $Fe(OH)_3$ can be further reduced at the cathode to form Fe_3O_4. The characteristics of Fe_3O_4 synthesized by this method, such as morphology, size, and size distribution, largely depend on several factors including the geometry of the electrochemical cell, electrode separation, current density, applied cell potential, temperature, and electrolyte composition.[72]

https://doi.org/10.1021/acs.chemmater.4c02013
Chem. Mater. 2024, 36, 9299−9319

In addition to the aforementioned method, a plethora of alternative synthesis techniques have been extensively explored, such as hydrothermal, sonochemical, and coprecipitation methods, among others.[75−77] The aqueous coprecipitation method remains one of the preferred methods for the high-yield production of water-dispersible Fe_3O_4 due to its cost-effectiveness, reduced time consumption, and ease of scalability for industrial applications (Figure 2a).[50] Moreover, it offers an

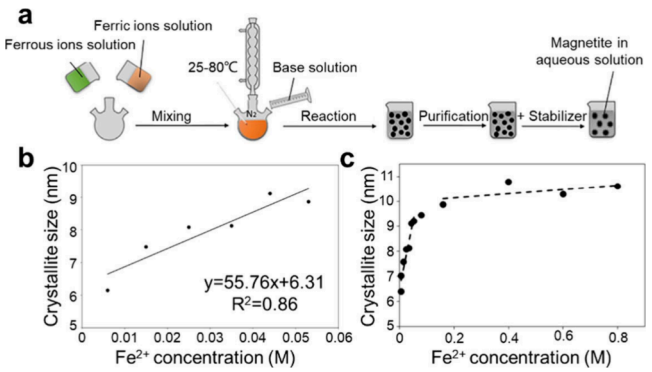

Figure 2. (a) Schematic representation of coprecipitation. Reproduced with permission from ref 50. Copyright 2022 Elsevier. (b) Average crystallite size versus Fe^{2+} for low concentration ($Fe^{2+} \leq 0.080$M). Reproduced with permission from ref 73. Copyright 2009 IOP Publishing. (c) Average crystallite size versus Fe^{2+} for $Fe^{2+} \leq 0.080$ M. Reproduced with permission from ref 74. Copyright 2010 IOP Publishing.

environmentally friendly approach by avoiding the use of hazardous solvents and reagents, as well as high reaction temperatures or pressures. This technique is based on the simultaneous precipitation of ferrous salts and ferric salts in an alkaline aqueous solution, as described by the following chemical equation:

$$Fe^{2+} + 2Fe^{3+} + 8OH^- \rightarrow Fe_3O_4 + 4H_2O$$

In a typical coprecipitation reaction, a mixture of salts is dissolved in water, and an alkali is added to the iron solution to induce precipitation. Ammonia or strong hydroxides are commonly used as alkalis to induce precipitation. Numerous reports have demonstrated that it is possible to control the diameter of the synthesized nanoparticles by regulating parameters such as precursor concentration, pH, temperature, stirring speed, and additives.

Takeuchi and Marschilok et al. conducted an in-depth study on the method of controlling the diameter of Fe_3O_4 nanoparticles in the coprecipitation method.[74] In contrast to previous reports that used ammonia or strong alkaline solutions, they opted for triethylamine due to its low volatility, which allows for precise concentration control, and its capability to form a buffer in aqueous solutions. Furthermore, their strategy effectively controls the microcrystal size without the need for restrictive media or complex apparatus. They observed that by varying the concentrations of ferrous and ferric ions, they could control the grain size of the magnetite product, finding a strong correlation between microcrystal size and concentration; higher concentrations led to larger microcrystals (Figure 2b). To gain deeper insight into the nucleation mechanisms during the synthesis of magnetite, they increased the concentration of ferrous in the solution (Figure 2c). They found that between 0.006 and 0.053 M, the microcrystal size linearly increased from 6 to 10 nm with concentration. However, between 0.080 and 0.800 M, there was no consistent increase in microcrystal size with increasing concentration.

As early as 1950, LaMer and colleagues proposed a mechanism for nucleation in nanomaterials, noting that the solution concentration increases until it reaches a critical level termed supersaturation.[78] At this supersaturation level, homogeneous nucleation occurs. The burst of homogeneous nucleation immediately reduces the supersaturation level in the solution, halting further nucleation. Subsequently, crystal growth occurs due to diffusion toward the nucleus. This mechanism has been widely applied to explain homogeneous nucleation and crystal growth. However, it does not fully account for the bimodal correlation between ferrous concentration and particle size in Fe_3O_4 nanomaterials. Another nucleation mechanism noted that impurities in the solution, or pre-existing substrates, could also serve as nucleation sites in the synthesis of nanomaterials.[79,80] Considering both scenarios, Takeuchi and Marschilok et al. suggested that in the synthesis of Fe_3O_4 nanomaterials, heterogeneous nucleation dominates at lower concentrations, while homogeneous nucleation prevails at higher concentrations.[74] At low concentrations, the concentration of ferric ions is too dilute to reach supersaturation, thus not triggering homogeneous nucleation. However, heterogeneous nucleation may occur in all reactions due to imperfections on the surface of glass vessels and the presence of minute amounts of dust in either the glassware or reaction solution. As nucleation remains constant, crystal growth effects dominate at lower concentrations. Thus, as iron concentration increases, microcrystal size also increases. At higher concentrations, the solution easily reaches supersaturation, hence the homogeneous nucleation mechanism is more active. According to LaMer's model, there is competition between nucleation and crystal growth. Therefore, as iron concentration increases, microcrystal size remains unchanged.

■ ELECTROCHEMICAL PROPERTIES

The essence of electrochemical performance relies on electron conduction and ion transport throughout the entire electrochemical system. Further, in a model ideal battery, the resistance associated with both electrons traveling from the external circuit through current collector and then to the active material, as well as ion transport between the electrolyte and the active material are considered relatively low. In that case, battery electrochemical performance largely depends on the intrinsic ability of the active materials to conduct electrons and ions. However, in real battery operation, the two resistances that are theoretically considered low can become quite fragile.[81] Various issues, such as the formation of insulating interfaces or the detachment of the electrode from the current collector, can invalidate these assumptions, leading to rapid deterioration of electrochemical performance.[3] In addition, in CTAMs such as Fe_3O_4, the reversible multiphase changes occurring during the movement of ions and electrons can easily result in the formation of crystal defects, causing isolated active material that can no longer participate in redox reactions. This section illustrates how to optimize Fe_3O_4 electrochemical performance by controlling electron/ion transport and the intrinsic properties of Fe_3O_4, and introducing external materials.

https://doi.org/10.1021/acs.chemmater.4c02013
Chem. Mater. 2024, 36, 9299−9319

Particle Size. Transitioning from the synthesis of Fe_3O_4 to its energy storage applications, it is first important to elucidate the impact of particle size on the materials' electrochemical performance to confirm the potential of Fe_3O_4 as an electrode-active material. These studies have greatly contributed to making Fe_3O_4 a popular candidate as a future anode material.[40] Nanoparticle size profoundly influences factors such as surface area, electronic structure and ionic pathways, where the latter is particularly crucial for materials like Fe_3O_4, that lack distinct layers or channels to facilitate Li^+ intercalation.[34] Conceptually, electrochemical lithiation is envisioned to proceed from the surface inward, imagined as a shrinking magnetite core surrounded by a reduced or partially reduced surface. Kinetic limitations such as slow Li^+ diffusion and resulting polarization may impact the functional capabilities of these systems.

In 2008, Komaba et al. synthesized Fe_3O_4 with particle sizes of 400, 100, and 10 nm to investigate the effect of particle size on the electrochemical activity within a voltage range of 4.0 V to 1.5 V.[82] The results indicated that the 400 nm Fe_3O_4 particles exhibited almost no electrochemical capacity (Figure 3a), whereas the 100 and 10 nm samples demonstrated

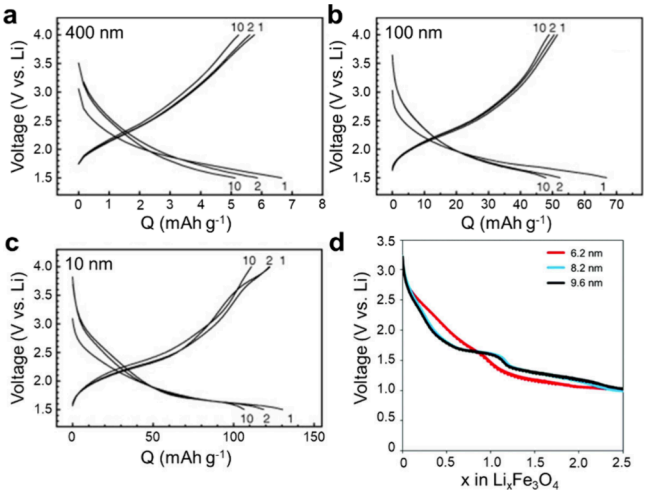

Figure 3. Galvanostatic discharge and charge curves of the Fe_3O_4 electrodes with the particle size of (a) 400, (b) 100, and (c) 10 nm. Reproduced with permission from ref 82. Copyright 2008 Elsevier. (d) Discharge voltage versus the lithiation status of electrodes with different Fe_3O_4 crystallite sizes. Reproduced with permission from ref 10. Copyright 2015 Royal Society of Chemistry.

significantly higher initial discharge capacity of approximately 70 mAh g^{-1} and 130 mAh g^{-1}, respectively (Figure 3b and c). Furthermore, no significant differences were observed in the charge−discharge curves among the three samples. The results suggest that the enhancement in electrochemical activity is not due to kinetic improvements, but rather attributable to the nanoscale effects characteristic of Fe_3O_4.

Subsequent research focused on smaller Fe_3O_4 nanoparticles, as exemplified by the work of Takeuchi and Marschilok et al., who investigated the electrochemical performance of Fe_3O_4 nanoparticles with diameters of 6.2, 8.2, and 9.6 nm.[73] Notably, electrode capacity increased as the particle diameter decreased, with the 6.2 nm Fe_3O_4 particles exhibiting a 200% increase in capacity compared with the larger 9.6 nm analogs. Moreover, when fabricated into an electrode, the two larger Fe_3O_4 particles displayed similar voltage curves, with a distinct voltage plateau observed around 1.7 V, whereas the smallest microcrystal size resulted in a smoother curve (Figure 3d). Building on the work of Delville and colleagues, who utilized band theory to conceptualize the smoother voltage distribution of nanocrystalline materials relative to their well-crystallized counterparts,[83] Takeuchi and Marschilok et al. suggested that the smaller-sized Fe_3O_4 nanoparticles have a higher number of surface defects (i.e., distorted coordination polyhedra and dangling bonds), which provide more subgap states thus reducing the energy gap between the conduction and valence bands. During discharge, Li^+ insertion fills these localized sub-bandgap states, allowing incremental changes to the electrode's Fermi energy without necessitating any substantial structural changes.[73]

The aforementioned research demonstrates that smaller Fe_3O_4 nanoparticles can typically store more Li^+, which is crucial for achieving high energy density LiBs. However, as the particle diameter decreases, the surface area and surface energy increase. The high surface area and significant surface energy lead to nanoparticle aggregation through physical and/or chemical interactions, which can affect the stability and reactive properties of the particles.[84−86] Thus, investigating the impact of aggregation as a function of nanoparticle size can provide further insights into the effects of particle size on battery performance.[87] Similar to the effect of particle size on electrochemical performance, aggregation can hinder ion transport between nanoparticles, especially for those at the center of the aggregate. Understanding the aggregate behavior and properties is essential for optimizing the design and functionality of nanoenhanced battery systems. Bock et al. investigated the aggregation behavior of 8 and 28 nm Fe_3O_4 nanoparticles and further explored the impact on electrochemical performance.[39] Transmission electron microscopy (TEM) was used to comprehensively evaluate Fe_3O_4 agglomeration, demonstrating that aggregate size was independent of particle size. From an electrochemical perspective, materials with smaller particle sizes but comparable aggregate sizes exhibited less polarization and higher energy transfer during charge/discharge cycles.

Particle Structure. Fe_3O_4 nanoparticle structure is another important factor to consider. Typically, different structures can be characterized based on their dimensionality:[88,89]

0D Fe_3O_4: particles that are confined to the nanoscale in all three spatial dimensions. Common 0D nanomaterials include nanoparticles and nanocrystals.

1D Fe_3O_4: particles that are macroscopic in one dimension but restricted to nanoscale dimensions in the other two. This category includes nanowires, nanotubes, and nanorods.

2D Fe_3O_4: particles that extend in two dimensions but are extremely thin in the third dimension. Notable examples include nanofilms, nanolayers, and nanoplates.

3D Fe_3O_4: particles that are not confined to the nanoscale in any dimension, meaning their size exceeds 100 nm in all three dimensions. This group includes polyhedra and hollow spheres.

To compare the differences in electrode performance between 0D and 1D Fe_3O_4, Wong and Marschilok et al. used a hydrothermal synthesis technique to access Fe_3O_4 nanorods.[90] At a low current density of 200 mA g^{-1}, both the nanorod and nanoparticle electrodes delivered very similar capacities of 1003 and 999 mAh g^{-1}. However, when the current density was increased to 800 mA g^{-1}, the nanorod electrode achieved a capacity of 807 mAh g^{-1}, compared to only 562 mAh g^{-1} for the nanoparticle alternative. When the

https://doi.org/10.1021/acs.chemmater.4c02013
Chem. Mater. 2024, 36, 9299−9319

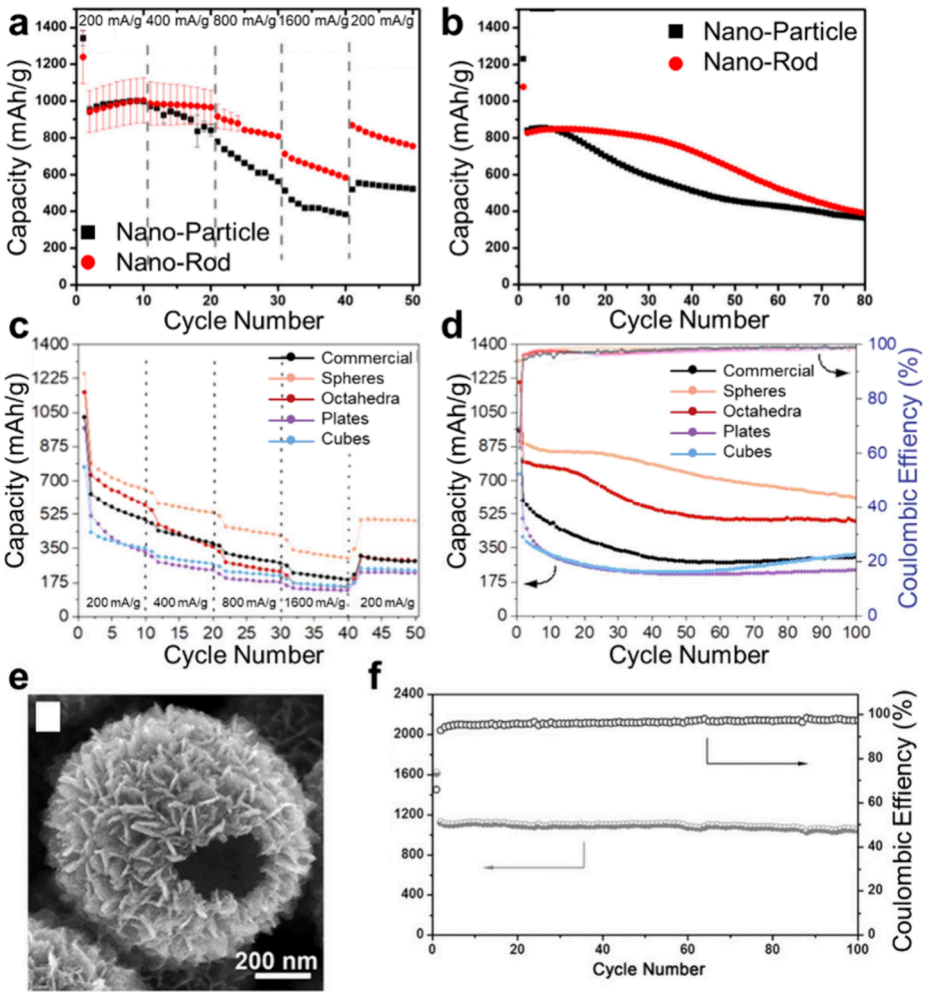

Figure 4. (a) Rate capability and (b) cycling stability for Fe_3O_4 nanorod and nanoparticle electrodes. Reproduced with permission from ref 90. Copyright 2019 American Chemical Society. (c) Rate capability and (d) cycling stability of the commercial and synthesized different structure Fe_3O_4 electrodes. Reproduced with permission from ref 91. Copyright 2022 IOP Publishing. (e) High-resolution SEM image of Fe_3O_4 hollow spheres organized by ultrathin nanosheets. (f) Cycling stability at a current density of 500 mA g^{-1}. Reproduced with permission from ref 92. Copyright 2015 John Wiley and Sons.

current density was reduced back to 200 mA g^{-1}, the nanoparticle electrode capacity recovered to 523 mAh g^{-1} (56% retention from cycles 2 to 50). In contrast, the nanorod electrode's capacity was 755 mAh g^{-1} (88% retention from cycles 2 to 50) (Figure 4a). The results suggest that Fe_3O_4 nanorod electrodes exhibit superior rate performance compared with their nanoparticle alternatives.

Interestingly, when cycled (Figure 4b), the Fe_3O_4 nanorod system exhibited an 88% capacity retention over the first 40 cycles, while the nanoparticle electrode only retained 61%. From the 40th to the 80th cycle, the nanorod electrode underwent faster capacity decay, eventually matching the nanoparticle electrode capacity by the 80th cycle. Electrochemical Impedance Spectroscopy (EIS) and Scanning Electron Microscopy (SEM) characterization before and after the cycling provided additional insights. The EIS results indicated that the as-prepared nanorod electrode exhibited slightly lower resistance, 9.7 ohms vs 12.6 ohms for the nanoparticle analog. After 50 cycles, the nanoparticle electrode showed only minor changes in resistance (13.1 ohms), whereas the resistance of the nanorod electrode increased significantly to 50.6 ohms. SEM imaging revealed that after 50 cycles, the nanoparticle electrode retained a morphology similar to its initial state.[90] This result is consistent with the increased charge transfer resistance derived from the EIS data. Additionally, structural changes and fragmentation caused by significant volumetric expansion during cycling were observed in the nanorod case. The results suggest that 1D nanorods demonstrate relatively weaker structural stability when subjected to volume changes caused by lithiation and delithiation. This is primarily due to their dimensional constraints limiting internal buffer space, which makes them more susceptible to structural fractures or stress accumulation during charge−discharge cycles.

Given these limitations, the question then arises as to whether 2D and 3D materials might offer optimized performance. The inherent structural advantages of 2D and 3D materials could potentially distribute stress more evenly across multiple directions, thereby limiting the fracture and enhancing overall material stability and performance. Wong et al. synthesized Fe_3O_4 nanomaterials with various structures (sphere, octahedral, plate, cube) using hydrothermal-based and microwave-assisted methods and compared them with commercial Fe_3O_4 nanoparticles.[91] Except for structural differences, high-resolution TEM was used to confirm the exposed facets of the various materials. The plates exhibited

https://doi.org/10.1021/acs.chemmater.4c02013
Chem. Mater. 2024, 36, 9299−9319

the (111) facets on their primary hexagonal surfaces and orthogonal (100) facets on their shorter dimensions. Octahedra displayed the (111) facets on all eight surfaces. Cubes showed the (100) facets on all six surfaces, and spheres displayed the (220) facets. Their rate capability results (Figure 4c) showed that the synthesized Fe_3O_4 spheres demonstrated the highest capacities across all current densities compared to other structures. Octahedra exhibited higher capacities at lower current density than the commercial Fe_3O_4 electrodes, but at higher current densities the capacities were similar. Cubes and plates consistently showed similar capacity, with both being lower than the alternative structures. During cycling (Figure 4d), the various samples displayed a similar trend, with the order of performance being sphere > octahedra > commercial > cube/plate.

The authors attributed the observed differences in electrochemical performance primarily to the particle crystallographic distinctions. A comparison between octahedra and cubes revealed that the (111) facets showed enhanced capacity retention compared to the (100) facets. Octahedra with the (111) facets provide higher capacity after 200 cycles than the cubes having (100) facets. However, SEM analyses revealed particularly severe aggregation in the plate samples, which is a potential reason for the performance of the plates—incorporating both (111) and (100) facets—approaching that of the cubes, which only contain the (100) facets. The findings also demonstrated the enhanced properties of the sphere samples, containing only the (220) facets, in terms of Fe_3O_4 oxidation and reduction, suggesting a higher quantity of electrochemically active sites could be present in higher index facets. Thus, the sphere structure, which exposes surfaces associated with the highest surface energy, should be the most stable and provide the highest capacity throughout extended cycling. In contrast, the commercial samples produced lower capacities, likely due to their larger size. However, their performance still surpassed that of plates and cubes containing the (100) facets.

To meet commercial application requirements, increasing the areal loading of active materials in the electrode is one method to enhance LiB energy density. However, high electrode mass loading leading to a high electrode thickness, which invariably introduces complex Li^+ transport pathways and slow charge transfer kinetics, results in different chemical reactions occurring at various depths of the electrode, causing rapid electrode capacity decay.[93] Reducing the tortuosity within the electrode is considered the most direct method to solve this issue, as low-tortuosity structures provide for the shortest Li^+ pathways.[94] The rational use of 2D Fe_3O_4, where the dimensions are restricted to nanoscale in one direction, allows for the fabrication of highly aligned, low-tortuosity electrodes. Yu et al. utilized the magnetic resonance properties of Fe_3O_4 itself to fabricate low-tortuosity Fe_3O_4 nanosheet electrodes with an areal loading as high as 25 mg cm^{-2}.[95] These electrodes demonstrated an areal capacity of up to 19 mAh cm^{-2} at a current density of 1.5 mA cm^{-2}. Even when the current density was increased to 15 mA cm^{-2}, the electrodes still achieved an areal capacity of 3.3 mAh cm^{-2}.

In addition to conventional nanostructures, exotic configurations can also yield unexpected benefits. For Fe_3O_4 nanomaterials, fabricating hollow spherical structures provides numerous advantages.[96] Hollow structures offer an increased surface area compared to solid particles, enhancing interactions between the active material and the external environment.[97] The internal space of hollow structures serves as a buffer to accommodate volume changes during lithiation/delithiation, thus mitigating structural damage during cycling and enhancing the electrode stability. Otherwise, due to their empty inner space, hollow structures are lighter than solid structures, which is a significant advantage for practical LiB applications. As an example, Lou et al. synthesized hollow Fe_3O_4 nanospheres composed of ultrathin nanosheets using a solvothermal method combined with calcination (Figure 4e).[92] The hollow structure assembled from 2D nanosheets retains the benefits of both the nanosheets and the hollow structure. For example, the nanosheets ensure short transport lengths for Li^+ and electrons, thereby improving rate performance. Additionally, the robust and well-defined hollow structure effectively adapts to severe volume changes during cycling. The cycling test result indicates that the nanosheet Fe_3O_4 hollow sphere electrode exhibits stable cycling performance over 100 cycles at a current density of 500 mA g^{-1} (Figure 4f). The initial discharge and charge capacity were ~1614 mAh g^{-1} and ~1063 mAh g^{-1}, respectively. A high reversible capacity of 1046 mAh g^{-1} was retained after 100 cycles, which is about 94% of the capacity in the second cycle.

Table 2 summarizes the electrochemical performance of Fe_3O_4 with different particle structures. Interestingly, for Fe_3O_4 electrodes, hollow structures tend to exhibit better rate and cycling performance. However, hollow structures inevitably impact the area/volume active material loading of the electrode, and this effect will be further amplified upon scaling to the whole battery, thereby affecting space utilization in practical applications. Compared to low-dimensional structures, 3D Fe_3O_4 particle structures generally show better cycling stability but poorer rate performance. Clearly, each structure has its own advantages and disadvantages, and their use should be described based on the specific application.

Table 2. Electrochemical Performance of Fe_3O_4-Based Electrodes with Different Particle Structures

structure	Fe_3O_4 content (%)	rate capacity (mAh g^{-1}) | current density or rate (mA g^{-1} or C)	cycling capacity (mAh g^{-1}) | # of cycles | current density or rate (mA g^{-1} or C)	ref
Nanorod	70	584 | 1600	388 | 100 | 200	90
Nanowire	60	906 | 500	503 | 100 | 500	98
Sphere	70	344 | 1600	609 | 100 | 200	91
Octahedra	70	≈175 | 1600	486 | 100 | 200	91
Plates	70	≈140 | 160	≈230 | 100 | 200	91
Cubes	70	≈175 | 1600	≈300 | 100 | 200	91
Polyhedra	50	500 | 1000	≈700 | 50 | 200	42
Hollow spheres	70	654.5 | 5	750 | 50 | 3	41
Hollow spheres (Plates)	70	457 | 10000	1046 | 100 | 500	92
Microflowers	80	≈825 | 1000	1000 | 50 | 100	99

Composite Electrode. The previous sections largely focused on optimizing Fe_3O_4 nanoparticle structure. However, the interactions between electrode materials components also critically determine battery capacity and stability.[100] Notably, agglomeration and the interactions between electrode materials impact battery capacity and stability. While previous studies have demonstrated that the aggregate size does not significantly influence the electrochemical properties,[39] the

https://doi.org/10.1021/acs.chemmater.4c02013
Chem. Mater. 2024, 36, 9299−9319

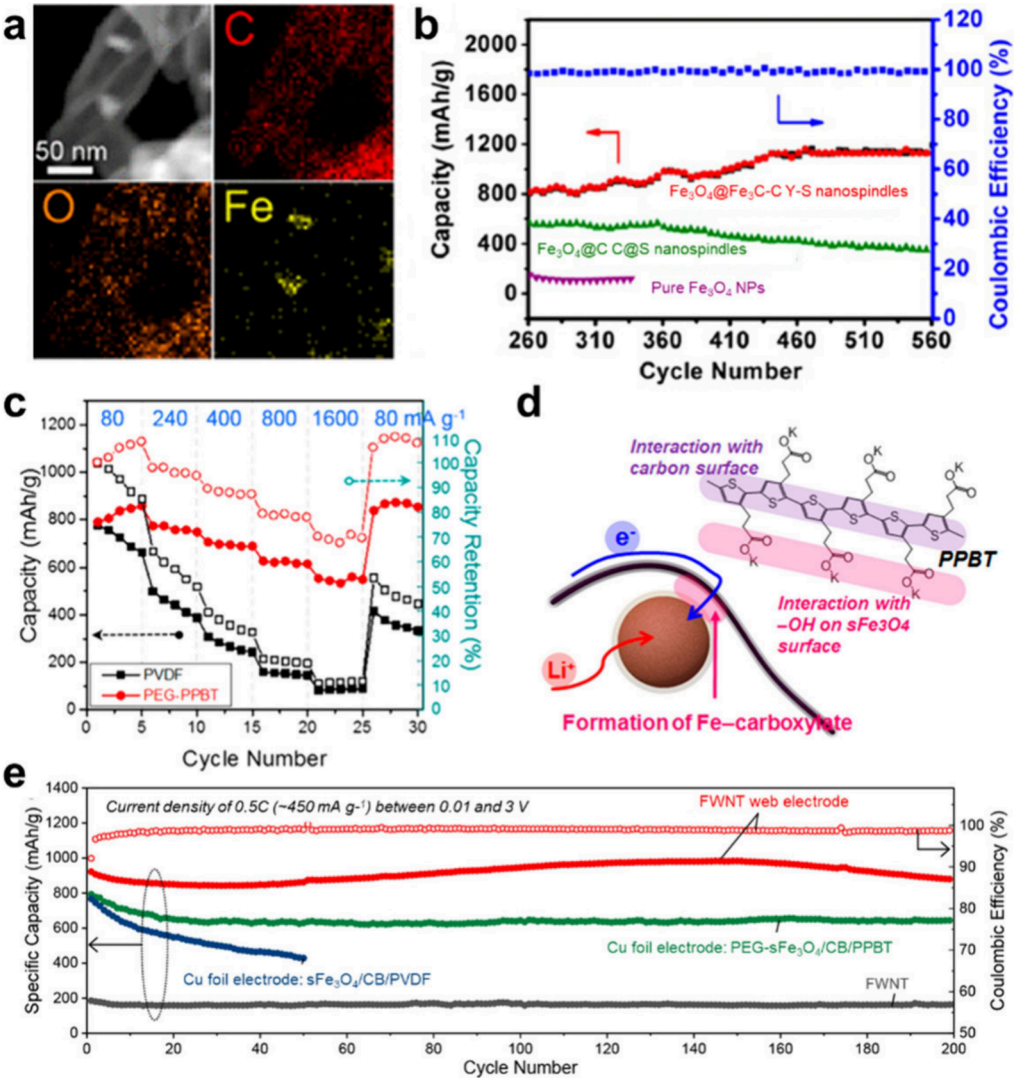

Figure 5. (a) TEM-EDS mapping of Fe_3O_4@ Fe_3C−C yolk−shell nanospindles. (b) Subsequent cycling tests of Fe_3O_4@Fe_3C−C yolk−shell nanospindles, Fe_3O_4@C core@shell nanospindles, and pure Fe_3O_4 NPs at 500 mA g^{-1} from the 261st to the 560th cycle. Reproduced with permission from ref 116. Copyright 2015 American Chemical Society. (c) Rate capability where cells were lithiated at a constant current density of 80 mA g^{-1} and delithiated at different current densities. Reproduced with permission from ref 117. Copyright 2016 American Chemical Society. (d) Schematics of the few-walled carbon nanotubes (FWNT) anchored with poly[3-(potassium butanoate)thiophene] (PPBT) links on Fe_3O_4. (e) Cycling stability collected for the current density of 0.5 C between 0.01 and 3 V. Reproduced with permission from ref 118. Copyright 2018 American Chemical Society.

occurrence of agglomeration inevitably increases the complexity of the interfaces between active materials. These, in turn, may impact overall electrochemical performance. The electrochemical behavior of the conversion electrodes is further complicated by the agglomeration of synthesized primary nanocrystals. Agglomeration occurs to accommodate the high surface energy of the nanomaterials, creating another size regime for which charge transfer needs to be considered. Continuum modeling has shown that the electrochemistry is impacted by the aggregation that provides an additional length scale for Li^+ transport.[101,102] Thus, characterizing agglomerate size and making correlations with its effects on electrochemical behavior is of interest. The use of ultramicrotome techniques have permitted the direct observation of agglomerates in large parallel sections (ca. 1 × 2 mm) of composite Fe_3O_4/carbon/binder electrodes, where imaging was performed using TEM and quantification of agglomerate size and dispersion was achieved using image processing software.[103] Furthermore, the use of 2D mapping by transmission X-ray microscopy and X-ray absorption near edge spectroscopy (XANES) provided a distribution of iron oxidation states in these electrodes both before and after electrochemical discharge.

Aggregation-controlled Fe_3O_4 composite electrodes were generated where Fe_3O_4 was dispersed in a carbon black matrix.[104] Galvanostatic cycling showed that Fe_3O_4 dispersion was initially beneficial in delivering a higher functional capacity, in agreement with continuum model simulations, but also results in increased capacity fade upon extended cycling, which is consistent with X-ray absorption spectroscopy (XAS) analysis of electrodes. Furthermore, higher charge-transfer resistance was observed for the dispersed nanoparticles compared to agglomerated Fe_3O_4, suggesting that increased solid electrolyte interphase (SEI) formation occurs on the dispersed, high-surface-area material and is detrimental to electrochemical behavior over extended cycling. Thus, dispersion of Fe_3O_4 is useful in initially facilitating ion

https://doi.org/10.1021/acs.chemmater.4c02013
Chem. Mater. 2024, 36, 9299−9319

transport, but the delivered capacity degrades with cycling illustrating the importance of interfacial control of the Fe_3O_4 surface.

For Fe_3O_4 active materials, the strategy of optimizing electrodes by inducing beneficial interactions between Fe_3O_4 and the external environment can be broadly categorized into three categories, namely with carbon, with polymer, and with both carbon and polymer.[43,45,105−107] Numerous studies have concentrated on understanding how interactions between different components affect the overall electrode performance. From a holistic perspective, optimizing Fe_3O_4 electrodes with carbon-based material primarily focuses on enhancing the conductivity of Fe_3O_4 nanoparticles through the high electron conductivity of carbon.[108,109] Additionally, some special structures such as core−shell and yolk−shell can limit the volume expansion of Fe_3O_4 during cycling, preventing electrode cracking and Fe_3O_4 particle pulverization.[110] Polymer optimization, except for the aforementioned advantages, also serves to enhance ionic conductivity and limits side reactions detrimental to the electrode.[111−113] The simultaneous optimization of Fe_3O_4 nanoparticles with carbon material and polymer can retain the advantages of both carbon and polymer additives, enhancing electrode performance comprehensively.[114,115]

Guo et al. synthesized Fe_3O_4 with a Fe_3C connected carbon yolk−shell structure (Fe_3O_4@Fe_3C−C Y−S) using a one-step *in situ* nanospace-confined pyrolysis strategy, where Fe_3O_4 nanoparticles were well combined within the compartments of hollow carbon nanospindles.[116] This unique structure introduces sufficient internal void space to accommodate the Fe_3O_4 volume changes, and provides dual shells of Fe_3C (the connection between Fe_3O_4 and the carbon shell) and carbon to limit Fe_3O_4 dissolution and volume changes. The dual protection strategy significantly enhanced the capacity retention. As shown in Figure 5a, the TEM Energy-Dispersive Spectroscopy (TEM-EDS) mapping images display a uniform distribution of C and O elements across the entire nanospindle, with Fe elements concentrated in the center of the nanospindle. The cycling data indicate that the capacity of the Fe_3O_4@Fe_3C−C Y−S electrode steadily increases (Figure 5b), reaching an impressive peak of 1128.3 mAh g^{-1}, with virtually no capacity decrease in the subsequent 100 cycles, ending with a capacity of 1120.2 mAh g^{-1}. In contrast, the capacity of the core−shell structured Fe_3O_4 particles (Fe_3O_4@C C@S) electrode ends far below that of the Fe_3O_4@Fe_3C−C Y−S system (365.4 mAh g^{-1}).

Compared to optimized Fe_3O_4 built with amorphous carbon shells, carbon nanotubes (CNTs) undoubtedly represent an attractive material option due to their superior mechanical properties.[119,120] Different from the amorphous carbon, CNTs can maintain structural integrity during a longer lithiation/delithiation period, and the high aspect ratio can establish a continuous conductive network throughout the composite electrode which contributes to the enhanced cycling stability and rate performance of the composites.[121] Zhao et al. developed a binder-free Fe_3O_4/CNTs/reduced graphene oxide (rGO) composite electrode through electrophoretic deposition.[122] The Fe_3O_4/CNTs/rGO electrode exhibited a discharge capacity of 1048 mAh g^{-1} after 50 cycles at a current density of 0.2 A g^{-1}, significantly higher than commercial Fe_3O_4 nanoparticle electrodes (174 mAh g^{-1}). The Coulombic efficiency (CE) of the Fe_3O_4/CNTs/rGO composite remained above 98% after the second cycle, whereas the commercial Fe_3O_4 electrodes only gradually increased to 98% by the 35th cycle. This demonstrated that the electrode stability and electronic conductivity of the Fe_3O_4/CNTs/rGO composite electrode are substantially enhanced vs Fe_3O_4 nanoparticle electrodes fabricated using commercial Fe_3O_4.

Another method for Fe_3O_4 interface optimization involves the use of polymer coatings, which through surface engineering promote synergistic interactions between the active material and the polymer interface. Traditional polymers used in battery electrodes, such as carboxymethyl cellulose (CMC),[123] polyvinylidene fluoride (PVDF),[124] and poly(acrylic acid) (PAA),[125] are electron/ion insulators, which limits the electron/ion transfer across the Fe_3O_4 interfaces. By incorporating polymers with electronic/ionic conductive polymers, ion transport channels can be formed around the Fe_3O_4 active material interface, thereby enhancing the diffusion dynamics of Li^+. These combined advantages ultimately improve the overall electrode performance.

Reichmanis et al. considered the benefits of both electron and ion transport in electrode design *via* incorporation of the conjugated polymer poly[3-(potassium butanoate)thiophene] (PPBT) as a binder while introducing a polyethylene glycol (PEG) coating layer on Fe_3O_4 nanoparticles (PEG-Fe_3O_4/PPBT).[117] As a traditional ion-conductive polymer, PEG can establish Li^+ transfer channels on the Fe_3O_4 surface, effectively improving Li^+ diffusion across the electrode surface. PPBT, serving as an electronic/ionic conducting polymer, establishes effective electronic bridges within the electrode system, facilitating more efficient electron transport. As shown in Figure 5c, the rate capability test demonstrated that under a constant lithiation current density of 80 mA g^{-1} (~0.1 C), electrodes based on the PEG-Fe_3O_4/PPBT binder exhibited superior rate capability across a wide range of delithiation current densities (from 80 to 1600 mA g^{-1}) within a voltage range of 0.01−3 V. This performance highlights their excellent ability to handle varying rates of charge and discharge. Additionally, other studies have demonstrated that introducing a polymer coating onto the Fe_3O_4 surface can effectively optimize the composition of the SEI, particularly via influencing the amounts of LiF and Li_2CO_3 formed during battery operation.[43,111,112]

As previously mentioned, considering Fe_3O_4, carbon and polymer simultaneously during the optimization of Fe_3O_4 could potentially achieve both increased capacity and extended battery life from a comprehensive perspective, however, integration of carbon nanotubes, polymers, and Fe_3O_4 may increase the complexity of electrode design. As an alternative, Reichmanis et al. coupled different components onto the Fe_3O_4 surface induced through grafting chemistry, resulting in the formation of a hybrid composite magnetite material (Figure 5d).[118] Specifically, PPBT is employed as a physical/chemical bridge connecting few-walled carbon nanotubes (FWNT) and Fe_3O_4. By inducing a reaction between PPBT and the abundant hydroxyl groups on the Fe_3O_4 metal oxide surface, PPBT can be chemically anchored to Fe_3O_4. Additionally, the π-conjugated polythiophene backbone of PPBT physically interacts with the π-electron-rich surfaces of two-dimensional graphene-like FWNT, thus establishing an FWNT web electrode. Despite the typical electrodes where polymers merely serve as a coating layer, the carboxylated polythiophene in PPBT facilitates the formation of extensive electronic pathways between Fe_3O_4 and FWNT through physical/chemical interactions. The FWNT web can constrain

https://doi.org/10.1021/acs.chemmater.4c02013
Chem. Mater. 2024, 36, 9299−9319

Table 3. Electrochemical Performance of Fe_3O_4 Electrodes within Different Composite Electrode Formulations

active material	Fe_3O_4 content (%)	rate capacity (mAh g^{-1}) | current density or rate (mA g^{-1} or C)	cycling capacity (mAh g-1) | # of cycles | current density or rate (mA g^{-1} or C)	ref
Fe_3O_4@graphite	80 (78% Fe_3O_4 + 18% graphite)	702 | 1000	≈840 | 40 | 100	126
Fe_3O_4@graphene	80	520 | 1750	≈ 580 | 100 | 700	46
Fe_3O_4-Multi Walled Carbon Nanotube	80 (50% Fe_3O_4 + 50% heterostructures)	522 | 2000	762 | 80 | Various	37
Carbon-Encapsulated Fe_3O_4	80 (68.7% Fe_3O_4)	311 | 20	556 | 350 | 10	110
Carbon Core−Shell Fe_3O_4	80 (65.9% Fe_3O_4)	250 | 10000	1120 | 560 | Various	116
Fe_3O_4@PEG	71.4 (90% Fe_3O_4)	≈550 | 1600	560 | 50 | 240	117
Fe_3O_4@Polypyrrole	70 (65.1% Fe_3O_4)	488 | 5	1278 | 200 | 0.5	127
Fe_3O_4@Polyaniline	80 (48.8% Fe_3O_4)	439 | 5000	1090 | 50 | 100	107
Fe_3O_4@graphene@PPy-C	80 (82.8% Fe_3O_4)	406 | 2000	724 | 320 | 200	128
Fe_3O_4@few walled carbon nanotube@PPBT	71.4 (63.6% Fe_3O_4)	≈770 | 3	880 | 200 | 0.5	118

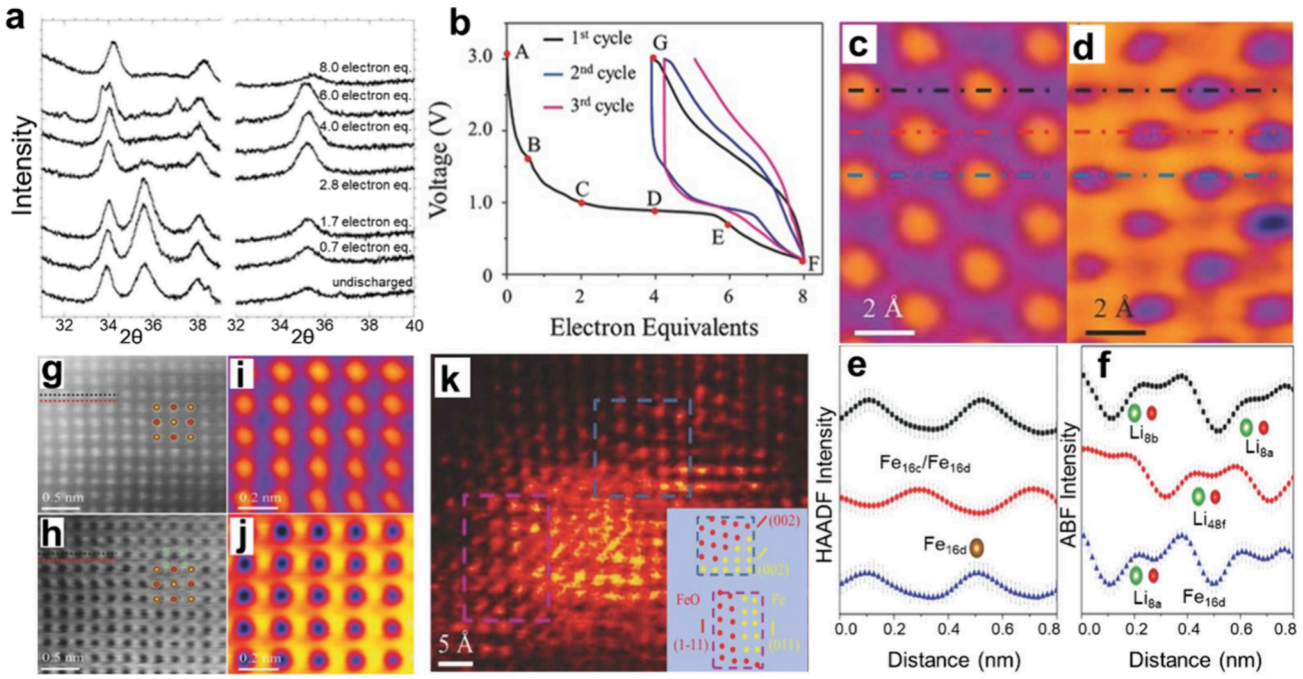

Figure 6. (a) X-ray diffraction of electrochemically reduced electrodes constructed using 10.6 nm Fe_3O_4 with electron equivalents indicated at 31−48° 2θ. Reproduced with permission from ref 129. Copyright 2013 Royal Society of Chemistry. (b) Voltage profiles of the binder-free Fe_3O_4/C electrode during galvanostatic cycling at a current rate equivalent to 1/80 C. Averaged HAADF (c) and ABF (d) images of Fe_3O_4 electrode discharged to two electron equivalents. (e,f) Intensity profiles from the line scan along the dashed lines in figures (c) and (d), respectively, showing the Li occupation at the 8a, 48f, and 8b sites. (g) HAADF and (h) ABF images from the same local region of the Fe_3O_4 particle viewed along the [100] direction. Atomic occupancy is illustrated in the inset (with brown, red, and green spheres representing the Fe, O, and Li atoms, respectively). Averaged (i) HAADF and (j) ABF images over one unit cell of Fe_3O_4. (k) A magnified HAADF image of the FeO/Fe nanoparticles, along with a schematic illustration of the atomic arrangements at two different interfacial areas as marked by the blue and pink boxes in panel. Reproduced with permission from ref 130. Copyright 2016 John Wiley and Sons.

the substantial volume changes of Fe_3O_4 during lithiation/delithiation processes, thereby enhancing electrode stability. The electrode cycling results (Figure 5e) demonstrate remarkably high cycle stability. Although a slight decay in capacity is observed in the initial cycles, the capacity gradually reaches a peak around the 140th cycle and only exhibits slow decay thereafter, exhibiting up to 95% capacity retention at the 200th cycle. Moreover, the FWNT web electrode consistently shows a higher capacity than other electrodes. In contrast, electrodes without FWNTs display only 81.2% capacity retention after 200 cycles, whereas traditional carbon black/PVDF electrodes experience rapid capacity decay within the first 50 cycles. Their work demonstrates that the simultaneous modification of Fe_3O_4 electrodes with polymers and carbon enhances multiple characteristics of the Fe_3O_4 electrodes. Furthermore, XPS analysis of the cycled electrodes, revealed a significantly increased LiF intensity and decreased Li_2CO_3 intensity in the FWNT web electrode.

Table 3 summarizes the performance of electrodes comprising Fe_3O_4 active material combined with various other materials. It provides the weight percentage of Fe_3O_4 in the active electrode material, and the types of other materials used. The rate and cycling stability of different composite electrodes are listed for reference. This article includes detailed information from selected studies to illustrate unique or representative synthesis and electrochemical results.

https://doi.org/10.1021/acs.chemmater.4c02013
Chem. Mater. 2024, 36, 9299−9319

CHARACTERIZATION METHOD

Advanced characterization methods, particularly the development of *in situ* characterization techniques, have greatly expanded the potential for Fe_3O_4 utilization in LiBs. In this section, we summarize and discuss how these advanced characterization techniques have driven the research and development of Fe_3O_4 materials for LiB applications.

The complex relationship between the Fe_3O_4 properties and battery performance requires intricate characterization tools to unveil the electrode material behavior during lithiation and delithiation processes. Some characterization techniques such as X-ray diffraction (XRD), XAS, and TEM have played a pivotal role in this regard. These methods provide critical insights into the structural, chemical and electrochemical transformations of Fe_3O_4 under different conditions, guiding researchers to optimize material design and significantly enhance battery performance. By highlighting the advanced characterization methods, we aim to emphasize their importance in deepening our understanding of Fe_3O_4 as a promising electrode material and in guiding the development of more robust, efficient, and durable LiBs.

***Ex Situ* Characterization.** When light is scattered by a periodic array with long-range order, it produces constructive interference at specific angles. XRD is based on the scattering of X-rays by the atoms in crystalline or partially crystalline materials. This scattering is collected by a detector and transformed into a diffraction pattern, which contains crystallographic information about the structure being analyzed. XRD data are collected over a range of scattering angles, and the diffraction pattern is a product of the materials' unique crystal structure, including its lattice parameters, crystal symmetry, and unit cell dimensions. This is crucial for understanding the electrochemical performance and stability of Fe_3O_4. Additionally, during the synthesis process, XRD can help with identifying and confirming the various phases present in the material; which in turn is important for optimizing synthesis conditions and enhancing material purity.

To investigate the microstructural changes of Fe_3O_4 materials at different electron equivalents, Takeuchi and Marschilok et al. characterized Fe_3O_4 electrodes with a 10.6 nm crystallite size under various electrochemical discharge levels using XRD (Figure 6a).[129] The powder patterns of the undischarged samples and those discharged to 0.7 and 1.7 electron equivalents showed similar peak combinations, which could be indexed to the cubic inverse spinel structure of magnetite. At the onset of the discharge through 1.7 electron equivalents, the electrochemically reduced Fe_3O_4 material has a spinel-like localized structure with iron ions in tetrahedral and octahedral environments. Between 2.8 and 4.0 electron equivalents, the iron atoms transform to occupy octahedral positions, consistent with a rock salt phase.

As a material capable of binding up to 8 electrons, Fe_3O_4 exhibits complex redox states and reactions. Although XRD can provide information on lattice changes, it analyzes the material from a macroscopic, holistic perspective. The development of annular bright-field (ABF) imaging enables direct observation of light elements such as H and Li. Wang and Takeuchi et al., combined ABF imaging with high-angle annular dark-field (HAADF) and electron energy loss spectroscopy (EELS) to directly detect all relevant anions (i.e., O^{2-}) and cations (Li^+, Fe^{2+}/Fe^{3+}) in the Fe_3O_4 discharge intermediate phases, providing detailed information on ion diffusion paths during the lithiation process.[130] Seven samples, located at the pristine status, 0.6, 2, 4, 6, and 8 electron equivalents, and one from a fully discharged and then fully charged electrode were interrogated (Figure 6b). Examination of the voltage profiles measured at the binder-free nano Fe_3O_4/C electrodes during the first three cycles (constant current mode) demonstrated that the behavior was irreversible during the first cycle, but reversible thereafter.

In electrodes discharged to 2−4 electron equivalents, intermediates containing rock salt units were formed. However, the rock salt structure typically does not allow for Li^+ insertion. To better understand Li^+ occupation and transport in the intermediates, atomic HAADF and ABF images (Figure 6c, d) of individual nanoparticles from samples discharged to 2 e^- and 4 e^- equivalents were recorded. In Figure 6c, d, bright and dark spots correspond to the positions of Fe ions, while other points with weaker contrast in the averaged ABF image reflect the positions of O^{2-} and Li^+. These points can be well distinguished on the averaged intensity distribution maps along the scan lines (dashed lines in Figure 6c, d) in Figure 6e, f. Based on the intensity distribution, the structure of lithiated Fe_3O_4 in the 2 e^- state was determined. Some Fe columns are entirely comprised of Fe 16c or Fe 16d, while other Fe columns are uniformly filled with Fe 16c and Fe 16d. However, the intensity of Fe columns is uniform throughout the unit cell, indicating that the proportion of Fe ions occupying the 16c sites is the same as that of the 16d sites. This equal occupation of Fe ions at the 16c and 16d sites bears similarities to the rock salt structure, resulting in the FeO-like phase.

In the 4 e^- sample, HAADF images show a uniform rock salt structure projected along the [100] direction, with no metallic Fe clusters detected. Figure 6g presents an enlarged HAADF image of a localized region within the nanoparticle, where all bright spots represent Fe/O columns, and Fe atoms remain at octahedral sites. Compared to the HAADF image, the ABF image from the same region reveals some new features (Figure 6h). In addition to the Fe/O columns with dark contrast, a faint but noticeable dark contrast at the tetrahedral sites (marked by green dots) can be observed. To clearly show these dark spots, the intensity of the whole HAADF and ABF images (in Figure 6g, h) was averaged to one unit cell of Fe_3O_4. The averaged images are given in Figure 6i, j. The slight reduction in intensity between the Fe/O columns clearly indicates the presence of lithium at the tetrahedral sites. Thus, the results suggest that further lithiation from 2 e^- equivalents to 4 e^- equivalents leads to increased lithium occupancy at the tetrahedral sites, specifically at the 8a and 48f sites initially, followed by the 8b sites.

With further lithiation (beyond 4 e^- equivalents), ultrafine Fe nanoparticles were produced. To elucidate the phase transformation process between Fe and FeO, atomic HAADF images were taken of the sample lithiated to 6 e^- equivalents (Figure 6k), revealing highly mixed Fe and FeO phases in localized regions. It provides a schematic illustration showing the arrangement of Fe atoms near the Fe/FeO interface. The Fe atomic columns of the Fe nanocrystals are marked with yellow spots in the center of the HAADF image, while the Fe atoms surrounding the FeO matrix are marked with red spots. This marking is directly obtained from two typical regions highlighted by green and pink boxes in the image. Because the atomic distances and bond angles on the (002) planes of Fe and FeO (as indicated by the blue box) are comparable, with a

https://doi.org/10.1021/acs.chemmater.4c02013
Chem. Mater. 2024, 36, 9299−9319

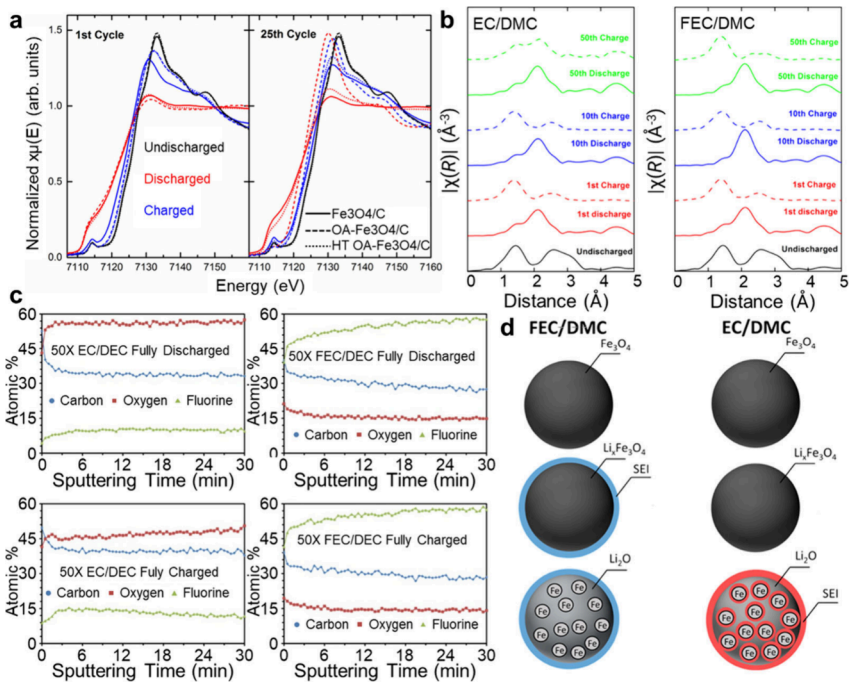

Figure 7. (a) XANES comparison of conventionally mixed Fe_3O_4/C, OA-Fe_3O_4/C, and HT OA-Fe_3O_4/C electrodes during the 1st and 25th cycles .Reproduced with permission from ref 131. Copyright 2016 American Chemical Society. (b) k^2-weighted $|\chi(R)|$ comparison of electrodes cycled in 1 M $LiPF_6$ 30:70 EC/DMC or 1 M $LiPF_6$ 30:70 FEC/DMC electrolyte during the first cycle (undischarged, full discharge and charge), 10th cycle (discharge and charge), and 50th cycle (discharge and charge). (c) Depth profile concentrations of C, O, and F for Fe_3O_4 electrodes cycled 50× in EC/DMC or FEC/DMC in the discharged and charged state. (d) Schematic of SEI formation on Fe_3O_4 electrodes as a function of discharge voltage for 1 M $LiPF_6$ 30:70 FEC/DMC and 1 M $LiPF_6$ 30:70 FEC/DMC electrolytes. Reproduced with permission from ref 132. Copyright 2018 American Chemical Society.

lattice mismatch of only about 6%, these two phases match very well at this interface.

Notably, the ccp O-anion array was maintained throughout the lithiation/delithiation process, enabling multiple lithium intercalation and conversion reactions. Slow cation replacement and reordering (within the ccp O-anion framework) lead to multiple phase transitions involving various intermediates, including a highly structurally integrated rock-salt-like phase $Li_xFe_3O_4$ and cation-segregated $Li_2O{\cdot}FeO$, and finally transitioned to a Fe/Li_2O nanocomposite phase, which then transforms to a FeO-like phase. The delithiation reaction produces a FeO-like phase rather than the original Fe_3O_4.

XAS is an element-specific technique that allows crystalline, amorphous, or nanocrystalline phases visualization. Different from the XRD technique, XAS does not rely on long-range periodic structures to obtain spectra. Specifically, XANES is a type of XAS. It refers to the absorption fine structure close to the absorption edge. This region typically exhibits the largest variations in X-ray absorption coefficients and is usually dominated by strong, narrow resonances. The technique provides information about the electronic structure of unoccupied energy levels. Takeuchi and Marschilok et al. utilized XAS-XANES to investigate the redox behaviors of Fe_3O_4 under different dispersion states.[131] Fe_3O_4 synthesized by coprecipitation was washed with acetone before drying and mixed with oleic acid (OA). After several hours of ultrasonic mixing, excess OA was washed with acetone to obtain well-dispersed OA-capped Fe_3O_4 (OA- Fe_3O_4). OA- Fe_3O_4 was then incorporated into carbon black in cyclohexane, isolated, and dried (OA- Fe_3O_4/C). Heat treatment was employed to remove the capping OA and keep the dispersed status (HT-OA- Fe_3O_4/C).

As shown in Figure 7a, three electrodes exhibited similar XANES plots under the undischarged state during the first charge and discharge process, indicating that the OA capping and heat treatment processes do not significantly influence the average Fe oxidation state. After first discharge, the XANES plots for all three electrode types exhibited a standard Fe metal XANES plot, indicating a predominantly Fe^0 oxidation state within the electrodes at this time. The minor discrepancies in the absorption edge profile between the three Fe_3O_4 samples suggest small changes in the local atomic environment. After charging, all three Fe_3O_4 sample types of positions returned to near 7.124 keV, indicating that all three electrodes returned to a state similar to that of FeO (7.121 keV). There is a slight difference between the highly dispersed samples (OA-Fe_3O_4/C and HT-OA-Fe_3O_4) and the conventionally mixed Fe_3O_4/C, with the XANES plots of the highly dispersed electrodes slightly shifted to higher energies, suggesting that at this point the Fe within the electrodes is being more completely oxidized. In the 25th cycle, the three electrodes showed significant differences. In the initial state, three XANES plots remained coincident, demonstrating that all three electrodes showed a similar reversibility in the previous 24 cycles. The HT OA-Fe_3O_4/C and Fe_3O_4/C electrodes exhibit reversibility between the 25th discharged and charged states. However, no significant changes were observed at the OA-Fe_3O_4/C electrode, which remained in a ferrous oxide state similar to that observed for the undischarged status.

Another variant of X-ray absorption spectroscopy is the extended X-ray absorption fine structure (EXAFS), which

https://doi.org/10.1021/acs.chemmater.4c02013
Chem. Mater. 2024, 36, 9299−9319

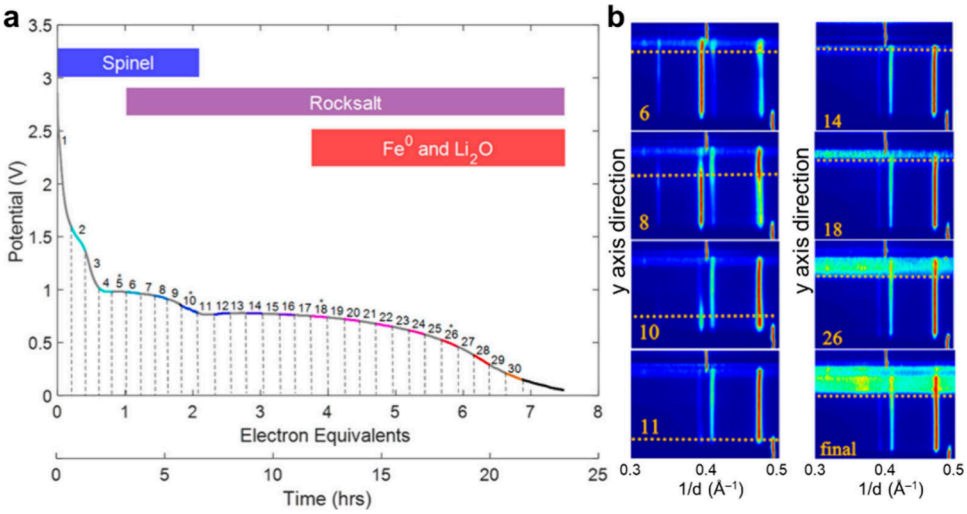

Figure 8. (a) Discharge voltage profile of a Li/Fe_3O_4 cell discharged at a C/25 rate. Contour plots shown in the figure correspond to the numbers identified on the discharge curve. (b) Contour plots for diffraction data from $1/d$ = 0.3 to 0.5 $Å^{-1}$, where the top of each contour plot corresponds to the Li/electrode interface, and the bottom of each contour plot corresponds to the electrode/current collector interface. Reproduced with permission from ref 135. Copyright 2019 American Chemical Society.

refers to the oscillatory portion of the absorption spectrum that begins approximately 50 eV beyond the absorption edge and extends up to about 1000 eV above it. By analyzing this region, it is possible to derive detailed local structural information about the specific atom under study. Takeuchi and Mansour et al. utilized EXAFS to conduct a comparative study of the cycling states of Fe_3O_4 in ethylene carbonate/dimethyl carbonate (EC/DMC) and fluoroethylene carbonate/DMC (FEC/DMC) electrolyte (Figure 7b).[132] For Fe_3O_4 electrodes in both electrolytes, the undischarged EXAFS spectra displayed main peaks centered at 1.4 Å, and 2.6 Å. The former one, was contributed by adjacent oxygen atoms coordinating with Fe in both octahedral and tetrahedral sites, and the latter primarily from contributions of neighboring iron atoms. At the first discharged state, the EXAFS spectra were dominated by a single broad peak centered at 2.1 Å, indicating a phase transition to metallic Fe^0. Upon charging to 3.0 V, the EXAFS spectra still consisted of two main peaks, which shifted in position and intensity relative to the undischarged Fe_3O_4, suggesting the electrode main form was a rock-salt-like FeO structure. By the 10th cycle, both electrodes demonstrated atomic structural reversibility, transitioning between Fe^0 and FeO-like structures. By the 50th cycle, the FEC/DEC electrode returned to a FeO-like structure after charging, while the EC/DMC electrode remained in the metallic Fe^0 state. This indicates that the majority of Fe centers within the electrode no longer participated in the electrochemical activity of lithium intercalation/deintercalation.

One of the most interesting properties of batteries is the formation of a SEI layer within the battery after initial cycling. SEIs occur when electrolyte reacts at the surface of the electrode causing a layer of byproduct to form.[133] Because the SEI layer is composed of decomposed electrolyte products onto the electrodes, different electrolyte/electrode compositions can lead to differing SEI layer compositions unique to each system. These SEI layers can often serve to protect the electrode from further parasitic reactions taking place under stable conditions, however, if the SEI layer is unstable, it will adhere poorly to the electrode causing depletion of the electrolyte by continuing to react and constantly forming insoluble products. Because of the complex and fragile nature of SEIs, the instrumentation required to analyze these layers are scarce.[134]

X-ray Photoelectron Spectroscopy (XPS) is a technique for analyzing the chemical composition of material surfaces. XPS measures the elemental composition as well as the chemical and electronic states of atoms within materials. To further investigate the effects of different electrolytes on Fe_3O_4 electrodes, XPS was employed to analyze the SEI layer. Regardless of the number of cycles, electrodes cycled in EC-based electrolytes exhibited more carbon−oxygen components, correlating with the presence of CO_3^{2-}, C═O, and C−O species in the SEI layer. Conversely, electrodes cycled in FEC-based electrolytes showed increased fluorine and lithium content, suggesting that the SEI layer in FEC electrolytes contains substantial amounts of LiF.

In further studies, argon ion sputtering was used to remove the outer layer of the SEI to explore the component change along the depth (Figure 7c). For electrodes cycled in EC-based electrolytes, the carbon content decreased with depth while fluorine and oxygen content increased. The composition of the SEI layer in discharged and charged states exhibited significant variations, indicating that the SEI composition of electrodes cycled in EC-based electrolytes is electrochemically reactive. In contrast, for electrodes cycled in FEC-based electrolytes, the carbon and oxygen content decreased with depth, and fluorine content increased. No significant changes were observed in the SEI composition in the discharged and charged states in FEC-based electrolytes, suggesting that the SEI formed in FEC electrolytes exhibits better stability.

As the sputtering depth increased, revealing the underlying electrode material, a peak at 51 eV binding energy was observed in EC-based electrolyte electrodes. This was attributed to Fe^0 which had been electrochemically isolated during cycling. Combined with XAS results, it was concluded that significant differences exist in the formation of the SEI layer on Fe_3O_4 electrodes in different electrolytes (Figure 7d). In FEC-based electrolytes, the formation of an SEI film at higher voltage can limit further electrolyte decomposition during lithiation, thus inhibiting the growth of the SEI layer on

https://doi.org/10.1021/acs.chemmater.4c02013
Chem. Mater. 2024, 36, 9299−9319

Fe^0 and Li_2O, and enhancing the reversibility of Fe^0. For electrodes in EC-based electrolytes, the formation of the SEI and the crystal transformation reactions of the electrode material Fe_3O_4 occur within the same voltage range, exposing some Fe^0 particles to the electrolyte and causing significant SEI growth, rendering these Fe^0 particles electrochemically inactive and unable to be oxidized to a FeO-like state.

***In Situ* Characterization.** As previously mentioned, *ex situ* experiments are typically conducted in standard laboratory environments without the need for complex equipment configurations. Additionally, since samples are removed from the reaction environment before measurement, the *ex situ* measured data is stable and reproducible. However, removing samples from the reaction environment may result in the loss of important information about reactive states or intermediate products. Furthermore, *ex situ* analysis cannot provide real-time information on electrode behavior during battery cycling, which is crucial for understanding the operational mechanisms and degradation of battery materials.

In recent years, *in situ* and *operando* characterization techniques have been developed and widely applied to track the real-time conditions of battery materials under various operating conditions, which offers a dynamic perspective that enhances the understanding of battery mechanisms. These characterization techniques are capable of observing transient processes and intermediate states in materials or chemical reactions, which are typically unobservable in *ex situ* experiments. Moreover, these experiments are operated under an approximately real battery working environment condition, which makes the results more representative.

In the study of Fe_3O_4, a typical *in situ*/*operando* technique employed is *in situ*/*operando* energy-dispersive X-ray diffraction (EDXRD). This method is different from the traditional XRD by using polychromatic photons as the light source, and typically operated at a fixed angle. *In situ*/*operando* EDXRD does not need an angle measuring device, thus, can rapidly collect complete diffraction patterns, facilitating the investigation of unstable materials or those that exist only for short periods. Since the entire spectrum of diffraction radiation is acquired simultaneously, it enables parallel data collection, allowing for the determination of structural changes over time.

Marschilok and West et al. utilized *in situ* EDXRD to thoroughly investigate the phase transformations during the Fe_3O_4 lithiation process.[135] Figure 8a shows the voltage profile of the Li/Fe_3O_4 cell, lithiated at a C/25 rate. Totally 30 *in situ* EDXRD measurements were operated during the Fe_3O_4 electrode lithiation process, dividing the voltage profile into 30 sections (Figure 8b). The top of each figure represents the diffraction patterns collected at the Li/electrode interface, while the bottom corresponds to those collected at the electrode/current collector interface. The number at the left bottom corner refers to the section during the lithiated process. From 0 to 1 electron equivalents discharge, no significant changes were observed, as the insertion of Li^+ at this stage does not alter the crystal structure of Fe_3O_4. During the discharge process from 1 to 2 e^- equivalents (Figure 8b, contour plots 6, 8, and 10), the intensity of the (311) peak in the spinel pattern of Fe_3O_4 ($1/d = 0.395$ $Å^{-1}$) decreased, and a new peak appeared at $1/d = 0.474$ $Å^{-1}$, which was identified as the (400) reflection of the rock salt phase. In figure number A 11, the electrode uniformly displayed the rock salt phase with no reflections corresponding to Fe_3O_4 observed. From 2 to 3 electron equivalents of discharge (Figure 8b, contour plots 11, and 14), the main crystalline phase in the electrode was the rock salt structure, with no significant changes in peak positions observed. However, around the discharge to four e^- equivalents (Figure 8b, contour plot 18), the intensity of reflections associated with the rock salt phase began to diminish in the electrode regions at the top side, indicating a transformation from rock salt to metallic Fe^0. As the discharge progressed (Figure 8b, contour plots 26 and final), distinct amorphous peaks were observed near the lithium metal, with the thickness of the peak bands increasing as the discharge progressed, indicating a gradual transformation of the rock salt phase into amorphous Li_2O and Fe^0 in the later stages of Fe_3O_4 battery discharge.

Interestingly, at the end of discharge, not all electrode area displayed an amorphous phase. The results were attributed the delayed or partial transformation from rock salt to amorphous phases Fe^0 and Li_2O to the limited diffusion of Li^+ through the electrode and the involvement of side reactions occurring at low potentials. During the transformation of the rock salt phase into Fe^0 and Li_2O, the electrochemical reaction propagated through the electrode until reaching the discharge voltage limit. The amorphous region did not spread throughout the entire electrode, resulting in an uneven distribution of phases. The observed results indicate that the diffusion of Li^+ through the electrode is the primary factor controlling transport within the electrode, and that this diffusion is further inhibited during the transformation process.

In-situ and *operando* TEM studies can provide valuable information to understand phase transitions and structural evolution during electrochemical reactions of conversion-type electrode materials for rechargeable ion batteries in lithium based battery systems, as reviewed by He et al.[136] A notable example from Su et al. used TEM to enable real-time visualization of the lithiation mechanism of Fe_3O_4 nanoparticles, revealing an overlap between intercalation and conversion reactions, which was not previously observed. The study employed a multifaceted approach, combining *in situ* strain-sensitive bright field scanning transmission electron microscopy (BF-STEM) imaging, density functional theory simulation, and phase-field simulation.[137] Specifically, HRTEM imaging was used to track the changes in crystal structure as Li^+ was intercalated into the Fe_3O_4 lattice, leading to the formation of the $LiFe_3O_4$ phase. This overlap suggests the importance of kinetic effects in influencing the lithiation process, shedding light on the complex electrochemical behavior of battery materials. Overall, the study underscores the significance of TEM techniques in unraveling fundamental mechanisms in battery research and highlights their role in kinetic effects and electrochemical conversion for magnetite nanoparticles.

An additional study by Li et al. revealed the structural evolution and electrochemical performance of Fe_3O_4 electrodes during cycling.[138] The study employed synchrotron XANES, electrochemical tests, and TEM to investigate the Fe_3O_4 electrodes. XANES analysis provided valuable information on the electronic and chemical state of iron during cycling, complementing the structural insights gained from TEM imaging. Electrochemical tests included rate capability tests and cyclic voltammetry. TEM observations explored the phase evolution, showing the formation of a composite of Li_2O and Fe nanoparticles during discharge, followed by incomplete reversal of the conversion reaction during charging. This incomplete reversal leads to the accumulation of Li_2O, acting

https://doi.org/10.1021/acs.chemmater.4c02013
Chem. Mater. 2024, 36, 9299−9319

as a kinetic barrier that hinders reversible electrochemical reactions. Additionally, TEM imaging highlights the thickening of passivation layers over cycles, which increases the diffusion length of charge carriers, thereby impacting the electrochemical kinetics at active sites. These TEM-based insights highlight understanding nanoscale structural changes in conversion-type electrodes for improving their cycling performance and guiding future materials design strategies.

The phenomenon of Fe_3O_4 exhibiting additional capacity beyond the theoretical limit in batteries has been a significant research focus.[140] This phenomenon has been widely reported in many studies, but the underlying mechanisms remain unclear. In 2002, Tarascon et al. suggested a possible correlation between the extra electrochemical capacity of metal oxide/lithium cells and the growth of a polymer or gel-like film around metallic (M^0) nanoparticles within a low discharge voltage range.[141] In later years, the interfacial storage theory was proposed, indicating that excess Li^+ ions can be accommodated at the M^0−Li_2O interfaces while electrons are confined to the metallic side. *Ex situ* solid-state NMR techniques were used to track the evolution of ^6Li, ^{17}O, and ^1H signals at different discharge states in the RuO_2/Li battery system, suggesting that the additional capacity likely originates from the reversible surface conversion of LiOH to Li_2O and LiH.[140] Recently, Li et al. utilized *in situ* XRD and *in situ* magnetometry to investigate the real-time evolution of the internal electronic structure in a typical Fe_3O_4/Li battery.[139] It was discovered that the reduced metallic Fe^0 in the Fe_3O_4/Li cell can continue to participate in the lithium storage reaction during the low voltage discharge process, as evidenced by a significant decrease in electrode magnetization.

Specifically, during the first discharge, when the potential dropped to 0.78 V, the inverse spinel structure of Fe_3O_4 transformed into a FeO-like rock-salt structure (Figure 9a). This observation is consistent with the discussions in this article. Correspondingly, the magnetization of the electrode rapidly decreased to 0.482 μB as the voltage decreased (Figure 9b). With further lithiation, the intensities of the (200) and (220) FeO-like diffraction peaks began to diminish, indicating a further transition from FeO to Fe^0. When the Fe_3O_4 electrode was fully lithiated, no pronounced XRD peaks were observed, implying that reduced products consisting of Fe^0 nanoparticles within the Li_2O matrix were not identifiable by XRD. Corresponding *in situ* magnetometry results showed that the magnetization significantly increased from 0.482 to 1.266 μB Fe^{1-} as the Fe_3O_4 electrode was discharged from 0.78 to 0.45 V, attributed to the conversion reaction from FeO to Fe^0. The magnetization then slowly decreased to 1.132 μB Fe^{1-} at the end of discharge. During the charging process, the magnetization increased with the rising voltage, reaching a maximum of 1.546 μB Fe^{1-} at approximately 1.4 V, and then decreased during subsequent delithiation. Further cycling tests indicated that this trend in change in magnetization with voltage was maintained in subsequent cycles, demonstrating that the process is reversible within the electrode. This finding suggests that fully reduced metallic Fe^0 nanoparticles may still participate in the lithium storage reaction, thus reducing the electrode magnetization, which contradicts the traditional understanding of conversion mechanisms in LIBs.

Considering the potential side reactions of the electrolyte at low voltage and the complexity of nanoparticle electrodes mixed with binders and conductive additives, Li et al. prepared Fe/TiO_2 composites with different nanoscale Fe particles and assembled them into thin-film batteries.[139] The cyclic voltammetry curves of the (Fe (1 nm)/TiO_2 (3 nm)) electrode exhibited a semirectangular shape, usually indicative of capacitive or pseudocapacitive behavior. Moreover, this electrode showed the same magnetization changes as observed in the low voltage region for the Fe_3O_4/Li cell. The authors suggested that these results indicate that the magnetization variation of the Fe_3O_4 electrode at low voltage is associated with the capacitive behavior of reduced Fe nanoparticles, which is believed to play a crucial role in the observed extra storage capacity. To investigate the phenomenon further, the electrodes were predischarged to 0.01 V and cyclic voltammetry measurements were obtained at various scan rates (Figure 9c). Rectangular cyclic voltammetry curves appeared in the voltage range between 0.01 and 1 V, indicating a capacitive response on the Fe_3O_4 electrode. To gain further insight, the variation of log I with log v was plotted, where I is the current and v is the scan rate. The slope of the curve, "*b*", is a kinetic parameter related to Li^+ diffusion. In LiBs, the *b* value typically ranges between 0.5 and 1. A *b* value close to 1 indicates that the reaction mechanism within the electrode is primarily controlled by the charge transfer process, meaning the electrode exhibits capacitive electrochemical behavior. As shown in Figure 9d, for scan rates ranging from 0.25 mV s^{-1} to 5 mV s^{-1}, the *b* values for both cathodic and anodic peaks were found to be equal to 1, indicating a capacitive response on the Fe_3O_4 electrode.

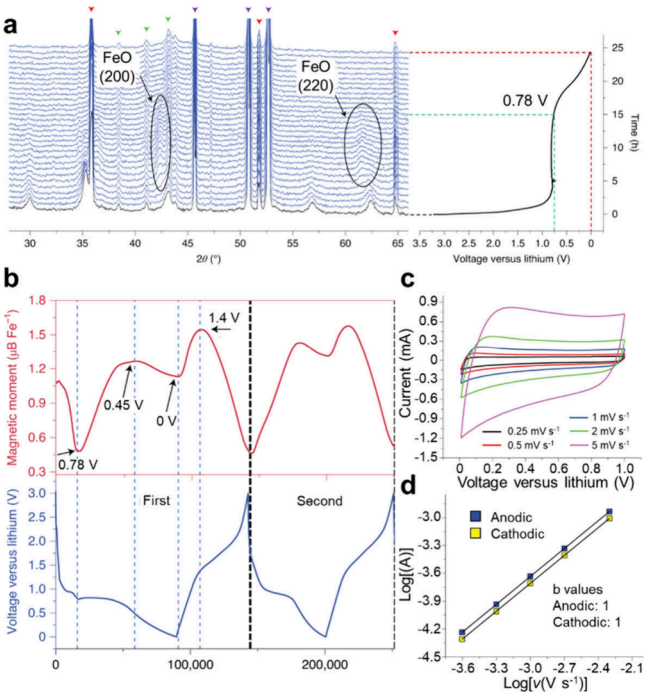

Figure 9. (a) *In situ* XRD patterns collected during the first discharge of an Fe_3O_4 electrode at a current density of 60 mA g^{-1} in the potential window between the OCV and 0.01 V. (b) *In situ* magnetometry in an Fe_3O_4/Li cell as a function of electrochemical cycling under an applied magnetic field of 3 T. (c) Cyclic voltammetry curves of an Fe_3O_4/Li cell that was discharged down to 0.01 V at various rates. (d) Determination of the *b* value by using the correlation between peak current and sweep rate. Reproduced with permission from ref 139. Copyright 2020 Springer Nature.

https://doi.org/10.1021/acs.chemmater.4c02013
Chem. Mater. 2024, 36, 9299−9319

CONCLUSION

This review has comprehensively covered the synthesis, electrochemical performance, composite formations, and characterization techniques of Fe_3O_4 as an active material in LiBs.

In the synthesis section, two primary methods for fabricating Fe_3O_4 nanoparticles were included. The top-down approach, such as ball milling, sputtering, and aerosol spray pyrolysis, starts with bulk magnetite and breaks it down into nanoparticles. In contrast, the bottom-up approach forms nanoparticles from molecular precursors under specific experimental conditions. Notable bottom-up techniques include thermal decomposition, microemulsion, sol−gel processes, and electrochemical synthesis. Among these, coprecipitation stands out for its simplicity, cost-effectiveness, and broad applicability. This method involves mixing metal salts with suitable precipitants under controlled temperature and pH conditions, allowing nanoparticles to coprecipitate from the solution. Among all these mentioned bottom-up synthesis methods, variables such as temperature, pH, reaction time, and stirring rate can be adjusted to influence the morphology, size, and distribution of the nanoparticles.

Subsequently, the impact of nanoparticle diameter on electrochemical performance was summarized. Typically, smaller diameters generally result in higher reversible capacities for Fe_3O_4 electrodes. This is thought to be the result of a combination of factors such as kinetic limitations and surface defects. Apart from the diameter, the Fe_3O_4 structures also served a crucial role in determining electrochemical performance. Different structures were categorized into 0D, 1D, 2D, and 3D types, and highlighted the unique properties of various shapes. By comparing the electrochemical properties of different types of Fe_3O_4 particles, it can be concluded that electrode electrochemical performance is highly correlated with the exposed Fe_3O_4 facets. Furthermore, 3D Fe_3O_4 particle structures generally exhibit better cycling stability, but poorer rate capability compared to lower-dimensional structures. Hollow structures tend to have better rate and cycling performance, but their disadvantage lies in the inevitable reduction of area/volume active material loading. Moreover, the review included the combination of Fe_3O_4 particles with other materials, especially carbon and polymer materials. These combinations aim to optimize the electrode performance by leveraging the benefits of both carbon and polymers. Carbon materials enhance the conductivity and mitigate volume expansion, while polymers improve ionic conductivity and limit side reactions. Some research findings also indicate that coupling with both carbon and polymers can optimize the active material from multiple dimensions.

Finally, the various characterization techniques applied to Fe_3O_4 electrode research were covered. *Ex situ* methods, such as XRD, provide fundamental insights into crystal structure changes, while TEM techniques (ABF and HAADF) offer detailed analysis on a smaller scale, revealing the complete reduction of Fe_3O_4 to Fe metal during the first discharge. XAS, often combined with XPS, is commonly used to study the reversible behavior and SEI formation in Fe_3O_4 electrodes. *In situ* techniques like EDXRD and *in situ* magnetic measurements provide dynamic insights into the structural and magnetic changes during cycling, elucidating the capacitive-like behavior at low voltages that contributes to the electrode's capacity exceeding its theoretical value.

Fe_3O_4 demonstrates significant potential as an active material in LiBs due to its diverse structural adaptability and the ability to form effective composites with other materials. However, to fully harness the potential of Fe_3O_4, several open questions remain to be addressed:

1. **Scalability and Manufacturing Processes:** Investigating the scalability of Fe_3O_4 synthesis methods and their integration into existing manufacturing processes is crucial for commercial application.
2. **Environmental Impact and Sustainability:** Assessing the environmental impact and sustainability of using Fe_3O_4 in LiBs can help ensure that the development of these materials aligns with global sustainability goals.
3. **Performance under Extreme Conditions:** Evaluating the performance of Fe_3O_4-based electrodes under extreme conditions, such as high or low temperatures, can provide insights into their robustness and reliability in various applications.
4. **Integration of Machine Learning and Computational Modeling:** Utilizing machine learning (ML) and computational modeling to inform experimental design can significantly accelerate the discovery and optimization of materials. ML models can predict material properties such as conductivity, ion diffusion coefficient, thermal stability, *etc.*, accelerating the discovery of new materials. By inputting material composition and structural parameters, ML models can predict key performance parameters such as capacity, cycle life, and efficiency.
5. **Advanced *in situ* Characterization Techniques:** Employing advanced *in situ* characterization techniques will be pivotal in monitoring the structural and chemical changes during battery operation. These techniques can guide the design of more robust and efficient electrode materials by providing real-time insights into their behavior.

It is noteworthy that, as a CTAM, many of the methods focused on Fe_3O_4 discussed in this review can be further extended to alternative conversion-type anode materials such as Mn_3O_4 and Co_3O_4. Additionally, transition metal fluorides/oxyfluorides have been widely studied as cathode active materials due to the high ionic nature of the bond between the metal and fluoride anions, which leads to a high reduction potential during the conversion reaction. In summary, the development of next-generation LiBs using more cost-effective, more environmentally friendly, and more efficient materials has been a shared goal of academia and industry for many years. By pioneering these advanced research directions and interdisciplinary approaches, the scientific community is moving forward toward revolutionizing energy storage solutions. The synergistic efforts in understanding and enhancing Fe_3O_4 as a pivotal component will not only push the boundaries of current battery technology but also pave the way for a sustainable and energy-efficient future.

AUTHOR INFORMATION

Corresponding Author

Elsa Reichmanis − *Department of Chemical and Bimolecular Engineering, Lehigh University, Bethlehem, Pennsylvania 18015, United States;* orcid.org/0000-0002-8205-8016; Email: elr420@lehigh.edu

https://doi.org/10.1021/acs.chemmater.4c02013
Chem. Mater. 2024, 36, 9299−9319

Authors

Haoze Ren − *Department of Chemical and Bimolecular Engineering, Lehigh University, Bethlehem, Pennsylvania 18015, United States;* orcid.org/0000-0002-0450-3962

Han Li − *Department of Chemical and Bimolecular Engineering, Lehigh University, Bethlehem, Pennsylvania 18015, United States;* orcid.org/0009-0003-1836-1381

Patrick Barry − *Institute of Energy: Sustainability, Environment and Equity, Stony Brook University, Stony Brook, New York 11794, United States; Department of Chemistry, Stony Brook University, Stony Brook, New York 11794, United States*

Zhongling Wang − *Institute of Energy: Sustainability, Environment and Equity, Stony Brook University, Stony Brook, New York 11794, United States; Department of Materials Science and Chemical Engineering, Stony Brook University, Stony Brook, New York 11794, United States;* orcid.org/0000-0003-3126-6189

Armando Rodriguez Campos − *Institute of Energy: Sustainability, Environment and Equity, Stony Brook University, Stony Brook, New York 11794, United States; Department of Chemistry, Stony Brook University, Stony Brook, New York 11794, United States*

Esther S. Takeuchi − *Institute of Energy: Sustainability, Environment and Equity, Stony Brook University, Stony Brook, New York 11794, United States; Department of Chemistry and Department of Materials Science and Chemical Engineering, Stony Brook University, Stony Brook, New York 11794, United States; Interdisciplinary Science Department, Brookhaven National Laboratory, Upton, New York 11973, United States;* orcid.org/0000-0001-8518-1047

Amy C. Marschilok − *Institute of Energy: Sustainability, Environment and Equity, Stony Brook University, Stony Brook, New York 11794, United States; Department of Chemistry and Department of Materials Science and Chemical Engineering, Stony Brook University, Stony Brook, New York 11794, United States; Interdisciplinary Science Department, Brookhaven National Laboratory, Upton, New York 11973, United States;* orcid.org/0000-0001-9174-0474

Shan Yan − *Institute of Energy: Sustainability, Environment and Equity, Stony Brook University, Stony Brook, New York 11794, United States; Interdisciplinary Science Department, Brookhaven National Laboratory, Upton, New York 11973, United States;* orcid.org/0000-0002-9715-9100

Kenneth J. Takeuchi − *Institute of Energy: Sustainability, Environment and Equity, Stony Brook University, Stony Brook, New York 11794, United States; Department of Chemistry and Department of Materials Science and Chemical Engineering, Stony Brook University, Stony Brook, New York 11794, United States; Interdisciplinary Science Department, Brookhaven National Laboratory, Upton, New York 11973, United States;* orcid.org/0000-0001-8129-444X

Complete contact information is available at: https://pubs.acs.org/10.1021/acs.chemmater.4c02013

Notes

The authors declare no competing financial interest.

■ ACKNOWLEDGMENTS

This work was performed as part of the Center for Mesoscale Transport Properties, an Energy Frontier Research Center supported by the U.S. Department of Energy, Office of Science, Basic Energy Sciences, under award #DE-SC0012673. E.R. also appreciates support from Lehigh University through funds associated with the Carl Robert Anderson Chair in Chemical Engineering. E.S.T. acknowledges support as the William and Jane Knapp Chair for Energy and the Environment at Stony Brook University

■ REFERENCES

(1) Gueon, D.; Gonzalez, M. A.; Takeuchi, K. J.; Takeuchi, E. S.; Marschilok, A. C.; Reichmanis, E. Understanding Interfacial Chemistry Interactions in Energy-Dense Lithium-Ion Electrodes. *Accounts of Materials Research* **2023**, *4* (2), 156−167.

(2) Wang, Y.; Zhang, Y.; Cao, D.; Ji, T.; Ren, H.; Wang, G.; Wu, Q.; Zhu, H. Designing Low Tortuosity Electrodes through Pattern Optimization for Fast-Charging. *Small Methods* **2023**, *7* (4), No. e2201344.

(3) Quilty, C. D.; Wu, D.; Li, W.; Bock, D. C.; Wang, L.; Housel, L. M.; Abraham, A.; Takeuchi, K. J.; Marschilok, A. C.; Takeuchi, E. S. Electron and Ion Transport in Lithium and Lithium-Ion Battery Negative and Positive Composite Electrodes. *Chem. Rev.* **2023**, *123* (4), 1327−1363.

(4) Jannesar Niri, A.; Poelzer, G. A.; Zhang, S. E.; Rosenkranz, J.; Pettersson, M.; Ghorbani, Y. Sustainability challenges throughout the electric vehicle battery value chain. *Renewable and Sustainable Energy Reviews* **2024**, *191*, 114176.

(5) Ershadi, M.; Javanbakht, M.; Kiaei, Z.; Torkzaban, H.; Mozaffari, S. A.; Ajdari, F. B. A patent landscape on Fe3O4/graphene-based nanocomposites in Lithium-Ion Batteries. *Journal of Energy Storage* **2022**, *46*, 103924.

(6) Chi, P. W.; Paul, T.; Su, Y. H.; Su, K. H.; Su, C. Y.; Wu, P. M.; Wang, S. F.; Wu, M. K. A study on Ti-doped Fe(3)O(4) anode for Li ion battery using machine learning, electrochemical and distribution function of relaxation times (DFRTs) analyses. *Sci. Rep* **2022**, *12* (1), 4851.

(7) Zhu, G.; Luo, D.; Chen, X.; Yang, J.; Zhang, H. Emerging Multiscale Porous Anodes toward Fast Charging Lithium-Ion Batteries. *ACS Nano* **2023**, *17* (21), 20850−20874.

(8) Wang, Y.; Cao, D.; Sun, X.; Ren, H.; Ji, T.; Jin, X.; Morse, J.; Stewart, B.; Zhu, H. Large-Scale Manufacturing of Pattern-Integrated Paper Li-Ion Microbatteries through Roll-to-Roll Flexographic Printing. *Advanced Materials Technologies* **2022**, *7* (11), 2200303.

(9) Sun, X.; Gao, G.; Yan, D.; Feng, C. Synthesis and electrochemical properties of Fe3O4@MOF core-shell microspheres as an anode for lithium ion battery application. *Appl. Surf. Sci.* **2017**, *405*, 52−59.

(10) Bruck, A. M.; Cama, C. A.; Gannett, C. N.; Marschilok, A. C.; Takeuchi, E. S.; Takeuchi, K. J. Nanocrystalline iron oxide based electroactive materials in lithium ion batteries: the critical role of crystallite size, morphology, and electrode heterostructure on battery relevant electrochemistry. *Inorganic Chemistry Frontiers* **2016**, *3* (1), 26−40.

(11) Wang, R.; Wang, L.; Liu, R.; Li, X.; Wu, Y.; Ran, F. "Fast-Charging" Anode Materials for Lithium-Ion Batteries from Perspective of Ion Diffusion in Crystal Structure. *ACS Nano* **2024**, *18* (4), 2611−2648.

(12) Li, A. M.; Wang, Z.; Pollard, T. P.; Zhang, W.; Tan, S.; Li, T.; Jayawardana, C.; Liou, S. C.; Rao, J.; Lucht, B. L.; Hu, E.; Yang, X. Q.; Borodin, O.; Wang, C. High voltage electrolytes for lithium-ion batteries with micro-sized silicon anodes. *Nat. Commun.* **2024**, *15* (1), 1206.

(13) He, C.; Wu, S.; Zhao, N.; Shi, C.; Liu, E.; Li, J. Carbon-Encapsulated Fe3O4 Nanoparticles as a High-Rate Lithium Ion Battery Anode Material. *ACS Nano* **2013**, *7* (5), 4459−4469.

(14) Zhang, J.; Yu, A. Nanostructured transition metal oxides as advanced anodes for lithium-ion batteries. *Science Bulletin* **2015**, *60* (9), 823−838.
(15) Yang, X.-G.; Liu, T.; Wang, C.-Y. Thermally modulated lithium iron phosphate batteries for mass-market electric vehicles. *Nature Energy* **2021**, *6* (2), 176−185.
(16) Yu, Y.; Karayaylali, P.; Giordano, L.; Corchado-Garcia, J.; Hwang, J.; Sokaras, D.; Maglia, F.; Jung, R.; Gittleson, F. S.; Shao-Horn, Y. Probing Depth-Dependent Transition-Metal Redox of Lithium Nickel, Manganese, and Cobalt Oxides in Li-Ion Batteries. *ACS Appl. Mater. Interfaces* **2020**, *12* (50), 55865−55875.
(17) Choi, S. H.; Ko, Y. N.; Lee, J. K.; Kang, Y. C. Rapid continuous synthesis of spherical reduced graphene ball-nickel oxide composite for lithium ion batteries. *Sci. Rep* **2014**, *4*, 5786.
(18) Kozawa, T.; Kitabayashi, F.; Fukuyama, K.; Naito, M. Carbon nanoparticle-entrapped macroporous Mn(3)O(4) microsphere anodes with improved cycling stability for Li-ion batteries. *Sci. Rep* **2022**, *12* (1), 11992.
(19) Ju, Z.; Zhang, B.; Zheng, T.; Marschilok, A. C.; Takeuchi, E. S.; Takeuchi, K. J.; Yu, G. Assembled MXene-Liquid Metal Cages on Silicon Microparticles as Self-Healing Battery Anodes. *Nano Lett.* **2024**, *24* (22), 6610−6616.
(20) Jang, J.; Song, S. H.; Kim, H.; Moon, J.; Ahn, H.; Jo, K. I.; Bang, J.; Kim, H.; Koo, J. Janus Graphene Oxide Sheets with Fe(3)O(4) Nanoparticles and Polydopamine as Anodes for Lithium-Ion Batteries. *ACS Appl. Mater. Interfaces* **2021**, *13* (12), 14786−14795.
(21) Wagemaker, M.; Mulder, F. M. Properties and Promises of Nanosized Insertion Materials for Li-Ion Batteries. *Acc. Chem. Res.* **2013**, *46* (5), 1206−1215.
(22) Li, N.; Sun, M.-Z.; Hwang, S.; Li, S.; Zhao, H.-Y.; Du, Y.-P.; Huang, B.-L.; Su, D. Non-equilibrium insertion of lithium ions into graphite. *Journal of Materials Chemistry A* **2021**, *9* (20), 12080−12086.
(23) Ohzuku, T.; Brodd, R. J. An overview of positive-electrode materials for advanced lithium-ion batteries. *J. Power Sources* **2007**, *174* (2), 449−456.
(24) Lu, Y.; Yu, L.; Lou, X. W. D. Nanostructured conversion-type anode materials for advanced lithium-ion batteries. *Chem.* **2018**, *4* (5), 972−996.
(25) Lu, S.; Wu, H.; Xu, S.; Wang, Y.; Zhao, J.; Li, Y.; Abdelkader, A. M.; Li, J.; Wang, W. A.; Xi, K.; Guo, Y.; Ding, S.; Gao, G.; Kumar, R. V. Iron Selenide Microcapsules as Universal Conversion-Typed Anodes for Alkali Metal-Ion Batteries. *Small* **2021**, *17* (8), No. e2005745.
(26) Zhu, J.; Ding, Y.; Ma, Z.; Tang, W.; Chen, X.; Lu, Y. Recent Progress on Nanostructured Transition Metal Oxides As Anode Materials for Lithium-Ion Batteries. *J. Electron. Mater.* **2022**, *51* (7), 3391−3417.
(27) Kraytsberg, A.; Ein-Eli, Y. A critical review-promises and barriers of conversion electrodes for Li-ion batteries. *J. Solid State Electrochem.* **2017**, *21*, 1907−1923.
(28) Pender, J. P.; Jha, G.; Youn, D. H.; Ziegler, J. M.; Andoni, I.; Choi, E. J.; Heller, A.; Dunn, B. S.; Weiss, P. S.; Penner, R. M.; Mullins, C. B. Electrode Degradation in Lithium-Ion Batteries. *ACS Nano* **2020**, *14* (2), 1243−1295.
(29) Bini, M.; Ambrosetti, M.; Spada, D. ZnFe2O4, a Green and High-Capacity Anode Material for Lithium-Ion Batteries: A Review. *Applied Sciences* **2021**, *11*, 11713.
(30) Pham, T. N.; Huy, T. Q.; Le, A.-T. Spinel ferrite (AFe2O4)-based heterostructured designs for lithium-ion battery, environmental monitoring, and biomedical applications. *RSC Adv.* **2020**, *10* (52), 31622−31661.
(31) Yu, S.; Hong Ng, V. M.; Wang, F.; Xiao, Z.; Li, C.; Kong, L. B.; Que, W.; Zhou, K. Synthesis and application of iron-based nanomaterials as anodes of lithium-ion batteries and supercapacitors. *Journal of Materials Chemistry A* **2018**, *6* (20), 9332−9367.
(32) Kong, X.; Shan, L.; Zhang, R.; Bao, S.; Tu, M.; Jia, R.; Yu, L.; Li, H.; Xu, B. Controllable engineering magnetite nanoparticles dispersed in a hierarchical amylose derived carbon and reduced graphene oxide framework for lithium-ion storage. *J. Colloid Interface Sci.* **2022**, *628* (Pt B), 1−13.
(33) Knehr, K. W.; Brady, N. W.; Lininger, C. N.; Cama, C. A.; Bock, D. C.; Lin, Z.; Marschilok, A. C.; Takeuchi, K. J.; Takeuchi, E. S.; West, A. C. Mesoscale Transport in Magnetite Electrodes for Lithium-Ion Batteries. *ECS Trans.* **2015**, *69* (1), 7.
(34) Huie, M. M.; Bock, D. C.; Bruck, A. M.; Tallman, K. R.; Housel, L. M.; Wang, L.; Thieme, J.; Takeuchi, K. J.; Takeuchi, E. S.; Marschilok, A. C. Isothermal Microcalorimetry: Insight into the Impact of Crystallite Size and Agglomeration on the Lithiation of Magnetite, Fe(3)O(4). *ACS Appl. Mater. Interfaces* **2019**, *11* (7), 7074−7086.
(35) Li, H.; Webster, T. J. Trends in nanomedicine. *Nanomedicine* **2023**, 1−18.
(36) Frey, P. A.; Reed, G. H. The ubiquity of iron. *ACS Chem. Biol.* **2012**, *7* (9), 1477−1481.
(37) Wang, L.; Li, Y. R.; Li, J.; Zou, S.; Stach, E. A.; Takeuchi, K. J.; Takeuchi, E. S.; Marschilok, A. C.; Wong, S. S. Correlating Preparative Approaches with Electrochemical Performance of Fe3O4-MWNT Composites Used as Anodes in Li-Ion Batteries. *ECS Journal of Solid State Science and Technology* **2017**, *6* (6), M3122−M3131.
(38) Wu, Q.; Jiang, R.; Mu, L.; Xu, S. Fe3O4 anodes for lithium batteries: Production techniques and general applications. *Comptes Rendus. Chimie* **2019**, *22* (1), 96−102.
(39) Bock, D. C.; Kirshenbaum, K. C.; Wang, J.; Zhang, W.; Wang, F.; Wang, J.; Marschilok, A. C.; Takeuchi, K. J.; Takeuchi, E. S. 2D Cross Sectional Analysis and Associated Electrochemistry of Composite Electrodes Containing Dispersed Agglomerates of Nanocrystalline Magnetite, Fe(3)O(4). *ACS Appl. Mater. Interfaces* **2015**, *7* (24), 13457−13466.
(40) Minnici, K.; Kwon, Y. H.; Huie, M. M.; de Simon, M. V.; Zhang, B.; Bock, D. C.; Wang, J.; Wang, J.; Takeuchi, K. J.; Takeuchi, E. S.; Marschilok, A. C.; Reichmanis, E. High capacity Li-ion battery anodes: Impact of crystallite size, surface chemistry and PEG-coating. *Electrochim. Acta* **2018**, *260*, 235−245.
(41) Xiong, Q. Q.; Tu, J. P.; Lu, Y.; Chen, J.; Yu, Y. X.; Qiao, Y. Q.; Wang, X. L.; Gu, C. D. Synthesis of Hierarchical Hollow-Structured Single-Crystalline Magnetite (Fe3O4) Microspheres: The Highly Powerful Storage versus Lithium as an Anode for Lithium Ion Batteries. *J. Phys. Chem. C* **2012**, *116* (10), 6495−6502.
(42) Su, D.; Horvat, J.; Munroe, P.; Ahn, H.; Ranjbartoreh, A. R.; Wang, G. Polyhedral magnetite nanocrystals with multiple facets: facile synthesis, structural modelling, magnetic properties and application for high capacity lithium storage. *Chemistry* **2012**, *18* (2), 488−497.
(43) Minnici, K.; Kwon, Y. H.; Housel, L. M.; Renderos, G. D.; Ponder, J. F.; Buckley, C.; Reynolds, J. R.; Takeuchi, K. J.; Takeuchi, E. S.; Marschilok, A. C.; Reichmanis, E. Tuning Conjugated Polymers for Binder Applications in High-Capacity Magnetite Anodes. *ACS Applied Energy Materials* **2019**, *2* (10), 7584−7593.
(44) Bruck, A. M.; Gannett, C. N.; Bock, D. C.; Smith, P. F.; Marschilok, A. C.; Takeuchi, K. J.; Takeuchi, E. S. The Electrochemistry of Fe3O4/Polypyrrole Composite Electrodes in Lithium-Ion Cells: The Role of Polypyrrole in Capacity Retention. *J. Electrochem. Soc.* **2017**, *164* (1), A6260−A6267.
(45) Bahadur, A.; Iqbal, S.; Shoaib, M.; Saeed, A. Electrochemical study of specially designed graphene-Fe(3)O(4)-polyaniline nanocomposite as a high-performance anode for lithium-ion battery. *Dalton Trans* **2018**, *47* (42), 15031−15037.
(46) Zhou, G.; Wang, D.-W.; Li, F.; Zhang, L.; Li, N.; Wu, Z.-S.; Wen, L.; Lu, G. Q.; Cheng, H.-M. Graphene-Wrapped Fe3O4 Anode Material with Improved Reversible Capacity and Cyclic Stability for Lithium Ion Batteries. *Chem. Mater.* **2010**, *22* (18), 5306−5313.
(47) Wang, Y.; Jin, Y.; Duan, Y.; Jia, M. Fe3O4 quantum dots on 3D-framed graphene aerogel as an advanced anode material in lithium-ion batteries. *Ionics* **2017**, *23* (8), 2005−2011.

https://doi.org/10.1021/acs.chemmater.4c02013
Chem. Mater. 2024, 36, 9299−9319

(48) Pilania, G.; Kocevski, V.; Valdez, J. A.; Kreller, C. R.; Uberuaga, B. P. Prediction of structure and cation ordering in an ordered normal-inverse double spinel. *Commun. Mater.* **2020**, *84* (1), 84.
(49) McKenna, K. P.; Hofer, F.; Gilks, D.; Lazarov, V. K.; Chen, C.; Wang, Z.; Ikuhara, Y. Atomic-scale structure and properties of highly stable antiphase boundary defects in Fe(3)O(4). *Nat. Commun.* **2014**, *5*, 5740.
(50) Niculescu, A. G.; Chircov, C.; Grumezescu, A. M. Magnetite nanoparticles: Synthesis methods - A comparative review. *Methods* **2022**, *199*, 16−27.
(51) Hamdallah, S. I.; Zoqlam, R.; Erfle, P.; Blyth, M.; Alkilany, A. M.; Dietzel, A.; Qi, S. Microfluidics for pharmaceutical nanoparticle fabrication: The truth and the myth. *Int. J. Pharm.* **2020**, *584*, 119408.
(52) Marcelo, G. A.; Lodeiro, C.; Capelo, J. L.; Lorenzo, J.; Oliveira, E. Magnetic, fluorescent and hybrid nanoparticles: From synthesis to application in biosystems. *Mater. Sci. Eng. C Mater. Biol. Appl.* **2020**, *106*, 110104.
(53) Hassani, A.; Karaca, M.; Karaca, S.; Khataee, A.; Acisli, O.; Yilmaz, B. Preparation of magnetite nanoparticles by high-energy planetary ball mill and its application for ciprofloxacin degradation through heterogeneous Fenton process. *J. Environ. Manage* **2018**, *211*, 53−62.
(54) Jamkhande, P. G.; Ghule, N. W.; Bamer, A. H.; Kalaskar, M. G. Metal nanoparticles synthesis: An overview on methods of preparation, advantages and disadvantages, and applications. *Journal of Drug Delivery Science and Technology* **2019**, *53*, 101174.
(55) Torres, W. S.; Alcantara, A. S.; Bini, R. D.; Alvim, M. B.; Santos, M. C.; Cótica, L. F.; Rocco, D. L. Top-down and bottom-up approaches to obtain magnetic nanoparticle of Fe3O4 compound: Pulsed laser deposition and chemical route. *Mater. Chem. Phys.* **2022**, *290*, 126511.
(56) Wu, J.; Shi, M.; Feng, F.; Hao, J.; Zhao, D.; Wang, X.; Li, J.; Zhang, W.; Wang, Q.; Ke, Y.; Yan, X.; Lin, Z.; Chai, L. Recent Advances in Magnetite Crystallization: Pathway, Modulation, and Characterization. *Cryst. Growth Des.* **2023**, *23* (8), 6201−6218.
(57) Laurent, S.; Forge, D.; Port, M.; Roch, A.; Robic, C.; Vander Elst, L.; Muller, R. N. Magnetic Iron Oxide Nanoparticles: Synthesis, Stabilization, Vectorization, Physicochemical Characterizations, and Biological Applications. *Chem. Rev.* **2008**, *108* (6), 2064−2110.
(58) Lu, A. H.; Salabas, E. L.; Schuth, F. Magnetic nanoparticles: synthesis, protection, functionalization, and application. *Angew. Chem., Int. Ed. Engl.* **2007**, *46* (8), 1222−1244.
(59) Zhang, M.; Lei, D.; Yin, X.; Chen, L.; Li, Q.; Wang, Y.; Wang, T. Magnetite/graphene composites: microwave irradiation synthesis and enhanced cycling and rate performances for lithium ion batteries. *J. Mater. Chem.* **2010**, *20* (26), 5538.
(60) Usman, M.; Byrne, J. M.; Chaudhary, A.; Orsetti, S.; Hanna, K.; Ruby, C.; Kappler, A.; Haderlein, S. B. Magnetite and Green Rust: Synthesis, Properties, and Environmental Applications of Mixed-Valent Iron Minerals. *Chem. Rev.* **2018**, *118* (7), 3251−3304.
(61) Montes-Hernandez, G.; Findling, N.; Renard, F. Direct and Indirect Nucleation of Magnetite Nanoparticles from Solution Revealed by Time-Resolved Raman Spectroscopy. *Cryst. Growth Des.* **2021**, *21* (6), 3500−3510.
(62) Sun, S.; Zeng, H. Size-Controlled Synthesis of Magnetite Nanoparticles. *J. Am. Chem. Soc.* **2002**, *124*, 8204−8205.
(63) Liu, S.; Yu, B.; Wang, S.; Shen, Y.; Cong, H. Preparation, surface functionalization and application of Fe(3)O(4) magnetic nanoparticles. *Adv. Colloid Interface Sci.* **2020**, *281*, 102165.
(64) Pereira, C.; Pereira, A. M.; Fernandes, C.; Rocha, M.; Mendes, R.; Fernández-García, M. P.; Guedes, A.; Tavares, P. B.; Grenèche, J.-M.; Araújo, J. P.; Freire, C. Superparamagnetic MFe2O4 (M = Fe, Co, Mn) Nanoparticles: Tuning the Particle Size and Magnetic Properties through a Novel One-Step Coprecipitation Route. *Chem. Mater.* **2012**, *24* (8), 1496−1504.
(65) Gu, T.; Zhang, Y.; Khan, S. A.; Hatton, T. A. Continuous Flow Synthesis of Superparamagnetic Nanoparticles in Reverse Mini-emulsion Systems. *Colloid and Interface Science Communications* **2019**, *28*, 1−4.
(66) Lu, T.; Wang, J.; Yin, J.; Wang, A.; Wang, X.; Zhang, T. Surfactant effects on the microstructures of Fe3O4 nanoparticles synthesized by microemulsion method. *Colloids Surf., A* **2013**, *436*, 675−683.
(67) Blanco-Andujar, C.; Ortega, D.; Pankhurst, Q. A.; Thanh, N. T. K. Elucidating the morphological and structural evolution of iron oxide nanoparticles formed by sodium carbonate in aqueous medium. *J. Mater. Chem.* **2012**, *22* (25), 12498.
(68) Hasany, S. F.; Ahmed, I.; J, R.; Rehman, A. Systematic Review of the Preparation Techniques of Iron Oxide Magnetic Nanoparticles. *Nanosci. Nanotechnol.* **2012**, *2* (6), 148−158.
(69) Parashar, M.; Shukla, V. K.; Singh, R. Metal oxides nanoparticles via sol-gel method: a review on synthesis, characterization and applications. *Journal of Materials Science: Materials in Electronics* **2020**, *31* (5), 3729−3749.
(70) Basavegowda, N.; Baek, K. H. Multimetallic Nanoparticles as Alternative Antimicrobial Agents: Challenges and Perspectives. *Molecules* **2021**, *26* (4), 912.
(71) Wallyn, J.; Anton, N.; Vandamme, T. F. Synthesis, Principles, and Properties of Magnetite Nanoparticles for In Vivo Imaging Applications-A Review. *Pharmaceutics* **2019**, *11* (11), 601.
(72) Lozano, I.; Casillas, N.; de León, C. P.; Walsh, F. C.; Herrasti, P. New Insights into the Electrochemical Formation of Magnetite Nanoparticles. *J. Electrochem. Soc.* **2017**, *164* (4), D184−D191.
(73) Zhu, S.; Marschilok, A. C.; Takeuchi, E. S.; Takeuchi, K. J. Crystallite Size Control and Resulting Electrochemistry of Magnetite, Fe3O4. *Electrochem. Solid-State Lett.* **2009**, *12* (4), A91−A94.
(74) Zhu, S.; Marschilok, A. C.; Takeuchi, E. S.; Yee, G. T.; Wang, G.; Takeuchi, K. J. Nanocrystalline Magnetite: Synthetic Crystallite Size Control and Resulting Magnetic and Electrochemical Properties. *J. Electrochem. Soc.* **2010**, *157* (11), A1158.
(75) Ravikumar, C.; Bandyopadhyaya, R. Mechanistic Study on Magnetite Nanoparticle Formation by Thermal Decomposition and Coprecipitation Routes. *J. Phys. Chem. C* **2011**, *115* (5), 1380−1387.
(76) Bracamonte, M. V.; Primo, E. N.; Luque, G. L.; Venosta, L.; Bercoff, P. G.; Barraco, D. E. Lithium dual uptake anode materials: crystalline Fe3O4 nanoparticles supported over graphite for lithium-ion batteries. *Electrochim. Acta* **2017**, *258*, 192−199.
(77) Shim, H. W.; Park, S.; Song, H. J.; Kim, J. C.; Jang, E.; Hong, K. S.; Kim, T. D.; Kim, D. W. Biomineralized Multifunctional Magnetite/Carbon Microspheres for Applications in Li-Ion Batteries and Water Treatment. *Chem.—Eur. J.* **2015**, *21* (12), 4655−4663.
(78) LaMer, V. K.; Dinegar, R. H. Theory, Production and Mechanism of Formation of Monodispersed Hydrosols. *J. Am. Chem. Soc.* **1950**, *72* (11), 4847−4854.
(79) WALTON, A. G. Nucleation of Crystals from Solution: Mechanisms of precipitation are fundamental to analytical and physiological processes. *Science* **1965**, *148* (3670), 601−607.
(80) Zheng, Y.-h.; Cheng, Y.; Bao, F.; Wang, Y.-s. Synthesis and magnetic properties of Fe3O4 nanoparticles. *Mater. Res. Bull.* **2006**, *41* (3), 525−529.
(81) Zheng, J.; Garcia-Mendez, R.; Archer, L. A. Engineering Multiscale Coupled Electron/Ion Transport in Battery Electrodes. *ACS Nano* **2021**, *15* (12), 19014−19025.
(82) Komaba, S.; Mikumo, T.; Ogata, A. Electrochemical activity of nanocrystalline Fe3O4 in aprotic Li and Na salt electrolytes. *Electrochem. Commun.* **2008**, *10* (9), 1276−1279.
(83) Kwon, C. W.; Quintin, M.; Mornet, S.; Barbieri, C.; Devos, O.; Campet, G.; Delville, M. H. Inorganic Nanocrystalline and Hybrid Nanocrystalline Particles (Gamma − Fe2 O 3/PPY) and Their Contribution to Electrode Materials for Lithium Batteries. *J. Electrochem. Soc.* **2004**, *151* (9), A1445−11559.
(84) Zhang, X.; Bruck, A. M.; Zhu, Y.; Peng, L.; Li, J.; Stach, E.; Zhu, Y.; Takeuchi, K. J.; Takeuchi, E. S.; Marschilok, A. C.; Yu, G. Probing enhanced lithium-ion transport kinetics in 2D holey nanoarchitectured electrodes. *Nano Futures* **2018**, *2* (3), 035008.
(85) Müller, S.; Eller, J.; Ebner, M.; Burns, C.; Dahn, J.; Wood, V. Quantifying Inhomogeneity of Lithium Ion Battery Electrodes and Its

Influence on Electrochemical Performance. *J. Electrochem. Soc.* **2018**, *165* (2), A339−A344.
(86) Zhu, M.; Park, J.; Sastry, A. M.; Lu, W. Numerical Study of Interaction and Aggregation of Non-Spherical Particles in Forming Li-Ion Battery Cathodes. *J. Electrochem. Soc.* **2014**, *161* (9), A1247−A1252.
(87) Lininger, C. N.; Brady, N. W.; West, A. C. Equilibria and Rate Phenomena from Atomistic to Mesoscale: Simulation Studies of Magnetite. *Acc. Chem. Res.* **2018**, *51* (3), 583−590.
(88) Zuo, X.; Zhu, J.; Müller-Buschbaum, P.; Cheng, Y.-J. Silicon based lithium-ion battery anodes: A chronicle perspective review. *Nano Energy* **2017**, *31*, 113−143.
(89) Su, X.; Wu, Q.; Li, J.; Xiao, X.; Lott, A.; Lu, W.; Sheldon, B. W.; Wu, J. Silicon-Based Nanomaterials for Lithium-Ion Batteries: A Review. *Adv. Energy Mater.* **2014**, *4* (1), 1300882.
(90) McBean, C. L.; Wang, L.; Moronta, D.; Scida, A.; Li, L.; Takeuchi, E. S.; Takeuchi, K. J.; Marschilok, A. C.; Wong, S. S. Examining the Role of Anisotropic Morphology: Comparison of Free-Standing Magnetite Nanorods versus Spherical Magnetite Nanoparticles for Electrochemical Lithium-Ion Storage. *ACS Applied Energy Materials* **2019**, *2* (7), 4801−4812.
(91) Salvatore, K. L.; Vila, M. N.; McGuire, S. C.; Hurley, N.; Huerta, C. R.; Takeuchi, E. S.; Takeuchi, K. J.; Marschilok, A. C.; Wong, S. S. Shape Dependence on the Electrochemistry of Uncoated Magnetite Motifs. *J. Electrochem. Soc.* **2022**, *169* (8), 080512.
(92) Ma, F. X.; Hu, H.; Wu, H. B.; Xu, C. Y.; Xu, Z.; Zhen, L.; David Lou, X. W. Formation of Uniform Fe3 O4 Hollow Spheres Organized by Ultrathin Nanosheets and Their Excellent Lithium Storage Properties. *Adv. Mater.* **2015**, *27* (27), 4097−4101.
(93) Ju, Z.; King, S. T.; Xu, X.; Zhang, X.; Raigama, K. U.; Takeuchi, K. J.; Marschilok, A. C.; Wang, L.; Takeuchi, E. S.; Yu, G. Vertically assembled nanosheet networks for high-density thick battery electrodes. *Proc. Natl. Acad. Sci. U. S. A.* **2022**, *119* (40), No. e2212777119.
(94) Zhang, X.; Ju, Z.; Housel, L. M.; Wang, L.; Zhu, Y.; Singh, G.; Sadique, N.; Takeuchi, K. J.; Takeuchi, E. S.; Marschilok, A. C.; Yu, G. Promoting Transport Kinetics in Li-Ion Battery with Aligned Porous Electrode Architectures. *Nano Lett.* **2019**, *19* (11), 8255−8261.
(95) Ju, Z.; Zhang, X.; Wu, J.; King, S. T.; Chang, C. C.; Yan, S.; Xue, Y.; Takeuchi, K. J.; Marschilok, A. C.; Wang, L.; Takeuchi, E. S.; Yu, G. Tortuosity Engineering for Improved Charge Storage Kinetics in High-Areal-Capacity Battery Electrodes. *Nano Lett.* **2022**, *22* (16), 6700−6708.
(96) Sheng, W.; Zhu, G.; Kaplan, D. L.; Cao, C.; Zhu, H.; Lu, Q. Silk-regulated hierarchical hollow magnetite/carbon nanocomposite spheroids for lithium-ion battery anodes. *Nanotechnology* **2015**, *26* (11), 115603.
(97) Lim, H.-S.; Jung, B.-Y.; Sun, Y.-K.; Suh, K.-D. Hollow Fe3O4 microspheres as anode materials for lithium-ion batteries. *Electrochim. Acta* **2012**, *75*, 123−130.
(98) Su, D.; Ahn, H.-J.; Wang, G. One-dimensional magnetite Fe3O4 nanowires as electrode material for Li-ion batteries with improved electrochemical performance. *J. Power Sources* **2013**, *244*, 742−746.
(99) Wang, X.; Liu, Y.; Arandiyan, H.; Yang, H.; Bai, L.; Mujtaba, J.; Wang, Q.; Liu, S.; Sun, H. Uniform Fe3O4 microflowers hierarchical structures assembled with porous nanoplates as superior anode materials for lithium-ion batteries. *Appl. Surf. Sci.* **2016**, *389*, 240−246.
(100) Ren, H.; Takeuchi, E. S.; Marschilok, A. C.; Takeuchi, K. J.; Reichmanis, E. Enhancing composite electrode performance: insights into interfacial interactions. *Chem. Commun. (Camb)* **2024**, *60*, 1979−1998.
(101) Knehr, K. W.; Brady, N. W.; Cama, C. A.; Bock, D. C.; Lin, Z.; Lininger, C. N.; Marschilok, A. C.; Takeuchi, K. J.; Takeuchi, E. S.; West, A. C. Modeling the Mesoscale Transport of Lithium-Magnetite Electrodes Using Insight from Discharge and Voltage Recovery Experiments. *J. Electrochem. Soc.* **2015**, *162* (14), A2817−A2826.
(102) Lininger, C. N.; Brady, N. W.; West, A. C. Equilibria and Rate Phenomena from Atomistic to Mesoscale: Simulation Studies of Magnetite. *Acc. Chem. Res.* **2018**, *51* (3), 583−590.
(103) Bock, D. C.; Kirshenbaum, K. C.; Wang, J.; Zhang, W.; Wang, F.; Wang, J.; Marschilok, A. C.; Takeuchi, K. J.; Takeuchi, E. S. 2D Cross Sectional Analysis and Associated Electrochemistry of Composite Electrodes Containing Dispersed Agglomerates of Nanocrystalline Magnetite, Fe3O4. *ACS Appl. Mater. Interfaces* **2015**, *7* (24), 13457−13466.
(104) Bock, D. C.; Pelliccione, C. J.; Zhang, W.; Wang, J.; Knehr, K. W.; Wang, J.; Wang, F.; West, A. C.; Marschilok, A. C.; Takeuchi, K. J.; Takeuchi, E. S. Dispersion of Nanocrystalline Fe3O4 within Composite Electrodes: Insights on Battery-Related Electrochemistry. *ACS Appl. Mater. Interfaces* **2016**, *8* (18), 11418−11430.
(105) Zhao, R.; Shen, X.; Wu, Q.; Zhang, X.; Li, W.; Gao, G.; Zhu, L.; Ni, L.; Diao, G.; Chen, M. Heterogeneous Double-Shelled Constructed Fe(3)O(4) Yolk-Shell Magnetite Nanoboxes with Superior Lithium Storage Performances. *ACS Appl. Mater. Interfaces* **2017**, *9* (29), 24662−24670.
(106) Chen, X.; Zhu, X.; Cao, G.; Zhang, S.; Mu, Y.; Ming, H.; Qiu, J. Fe3O4-Based Anodes with High Conductivity and Fast Ion Diffusivity Designed for High-Energy Lithium-Ion Batteries. *Energy Fuels* **2021**, *35* (2), 1810−1819.
(107) Wang, X.; Liu, Y.; Han, H.; Zhao, Y.; Ma, W.; Sun, H. Polyaniline coated Fe3O4 hollow nanospheres as anode materials for lithium ion batteries. *Sustainable Energy & Fuels* **2017**, *1* (4), 915−922.
(108) Xiang, J.; Wei, Y.; Zhong, Y.; Yang, Y.; Cheng, H.; Yuan, L.; Xu, H.; Huang, Y. Building Practical High-Voltage Cathode Materials for Lithium-Ion Batteries. *Adv. Mater.* **2022**, *34* (52), No. e2200912.
(109) Fang, R.; Chen, K.; Yin, L.; Sun, Z.; Li, F.; Cheng, H. M. The Regulating Role of Carbon Nanotubes and Graphene in Lithium-Ion and Lithium-Sulfur Batteries. *Adv. Mater.* **2019**, *31* (9), No. e1800863.
(110) He, C.; Wu, S.; Zhao, N.; Shi, C.; Liu, E.; Li, J. Carbon-Encapsulated Fe3O4 Nanoparticles as a High-Rate Lithium Ion Battery Anode Material. *ACS Nano* **2013**, *7* (5), 4459−4469.
(111) Gonzalez, M.; Minnici, K.; Risteen, B.; Wang, L.; Housel, L. M.; Renderos, G. D.; Takeuchi, K. J.; Takeuchi, E. S.; Marschilok, A. C.; Fuller, T. F.; Reichmanis, E. Active Material Interfacial Chemistry and Its Impact on Composite Magnetite Electrodes. *ACS Applied Energy Materials* **2021**, *4* (9), 9836−9847.
(112) Minnici, K.; Kwon, Y. H.; O'Neil, J.; Wang, L.; Dunkin, M. R.; Gonzalez, M. A.; Huie, M. M.; de Simon, M. V.; Takeuchi, K. J.; Takeuchi, E. S.; Marschilok, A. C.; Reichmanis, E. Carboxylated Poly(thiophene) Binders for High-Performance Magnetite Anodes: Impact of Cation Structure. *ACS Appl. Mater. Interfaces* **2019**, *11* (47), 44046−44057.
(113) Na, R.; Minnici, K.; Zhang, G.; Lu, N.; Gonzalez, M. A.; Wang, G.; Reichmanis, E. Electrically Conductive Shell-Protective Layer Capping on the Silicon Surface as the Anode Material for High-Performance Lithium-Ion Batteries. *ACS Appl. Mater. Interfaces* **2019**, *11* (43), 40034−40042.
(114) Kwon, Y. H.; Minnici, K.; Lee, S. R.; Zhang, G.; Takeuchi, E. S.; Takeuchi, K. J.; Marschilok, A. C.; Reichmanis, E. SWNT Networks with Polythiophene Carboxylate Links for High-Performance Silicon Monoxide Electrodes. *ACS Applied Energy Materials* **2018**, *1* (6), 2417−2423.
(115) Kwon, Y. H.; Minnici, K.; Park, J. J.; Lee, S. R.; Zhang, G.; Takeuchi, E. S.; Takeuchi, K. J.; Marschilok, A. C.; Reichmanis, E. SWNT Anchored with Carboxylated Polythiophene "Links" on High-Capacity Li-Ion Battery Anode Materials. *J. Am. Chem. Soc.* **2018**, *140* (17), 5666−5669.
(116) Zhang, J.; Wang, K.; Xu, Q.; Zhou, Y.; Cheng, F.; Guo, S. Beyond Yolk-Shell Nanoparticles: Fe3O4@Fe3C Core@Shell Nanoparticles as Yolks and Carbon Nanospindles as Shells for Efficient Lithium Ion Storage. *ACS Nano* **2015**, *9* (3), 3369−3376.
(117) Kwon, Y. H.; Minnici, K.; Huie, M. M.; Takeuchi, K. J.; Takeuchi, E. S.; Marschilok, A. C.; Reichmanis, E. Electron/Ion

Transport Enhancer in High Capacity Li-Ion Battery Anodes. *Chem. Mater.* **2016**, *28* (18), 6689−6697.
(118) Kwon, Y. H.; Park, J. J.; Housel, L. M.; Minnici, K.; Zhang, G.; Lee, S. R.; Lee, S. W.; Chen, Z.; Noda, S.; Takeuchi, E. S.; Takeuchi, K. J.; Marschilok, A. C.; Reichmanis, E. Carbon Nanotube Web with Carboxylated Polythiophene "Assist" for High-Performance Battery Electrodes. *ACS Nano* **2018**, *12* (4), 3126−3139.
(119) Luo, Y.; Wang, K.; Li, Q.; Fan, S.; Wang, J. Macroscopic Carbon Nanotube Structures for Lithium Batteries. *Small* **2020**, *16* (15), No. e1902719.
(120) Wu, Y.; Zhao, X.; Shang, Y.; Chang, S.; Dai, L.; Cao, A. Application-Driven Carbon Nanotube Functional Materials. *ACS Nano* **2021**, *15* (5), 7946−7974.
(121) Zhu, Z.; Cui, C.; Bai, Y.; Gao, J.; Jiang, Y.; Li, B.; Wang, Y.; Zhang, Q.; Qian, W.; Wei, F. Advances in Precise Structure Control and Assembly toward the Carbon Nanotube Industry. *Adv. Funct. Mater.* **2022**, *32* (11), 2109401.
(122) Yang, Y.; Li, J.; Chen, D.; Zhao, J. A Facile Electrophoretic Deposition Route to the Fe(3)O(4)/CNTs/rGO Composite Electrode as a Binder-Free Anode for Lithium Ion Battery. *ACS Appl. Mater. Interfaces* **2016**, *8* (40), 26730−26739.
(123) Ren, H.; Wang, Y.; Cao, D.; Gedney, W.; Ji, T.; Sun, X.; Zhu, H. Manufacturing Water-Based Low-Tortuosity Electrodes for Fast-Charge through Pattern Integrated Stamping. *Energy & Environmental Materials* **2023**, *6*, No. e12584.
(124) Wang, Y.; Mijailovic, A. S.; Ji, T.; Cakmak, E.; Zhao, X.; Huang, L.; Sheldon, B. W.; Zhu, H. Promoting electrochemical rates by concurrent ionic-electronic conductivity enhancement in high mass loading cathode electrode. *Energy Storage Materials* **2024**, *71*, 103546.
(125) Gonzalez, M. A.; Freer, W. H.; Wang, M.; Jeon, S.; Fuller, T.; Takeuchi, E. S.; Takeuchi, K. J.; Marschilok, A.; Reichmanis, E. Understanding the Role of Polymer Interactions within Binders in Composite Lithium-Ion Anodes. *J. Phys. Chem. C* **2022**, *126* (46), 19603−19617.
(126) Zeng, Z.; Zhao, H.; Wang, J.; Lv, P.; Zhang, T.; Xia, Q. Nanostructured Fe3O4@C as anode material for lithium-ion batteries. *J. Power Sources* **2014**, *248*, 15−21.
(127) Chu, R.; Tan, D.; Zhang, J.; Chen, Y.; Jiang, H.; Lin, J.; Li, L.; Zhang, Y.; Guo, H. Long-term cycling of core-shell Fe3O4-Polypyrrole composite electrodes via diffusive and capacitive lithiation. *J. Alloys Compd.* **2020**, *835*, 155192.
(128) Liu, Y.; Miao, X.; Zhang, X.; Chen, S.; Chen, Y.; Cheng, J.; Wang, W.; Zhang, Y. Targeted interfacial anchoring and wrapping of Fe3O4 nanoparticles onto graphene by PPy-derived-carbon for stable lithium-ion battery anodes. *Mater. Res. Bull.* **2019**, *111*, 170−176.
(129) Menard, M. C.; Takeuchi, K. J.; Marschilok, A. C.; Takeuchi, E. S. Electrochemical discharge of nanocrystalline magnetite: structure analysis using X-ray diffraction and X-ray absorption spectroscopy. *Phys. Chem. Chem. Phys.* **2013**, *15* (42), 18539−18548.
(130) Zhang, W.; Bock, D. C.; Pelliccione, C. J.; Li, Y.; Wu, L.; Zhu, Y.; Marschilok, A. C.; Takeuchi, E. S.; Takeuchi, K. J.; Wang, F. Insights into Ionic Transport and Structural Changes in Magnetite during Multiple-Electron Transfer Reactions. *Adv. Energy Mater.* **2016**, *6* (10), 1502471.
(131) Bock, D. C.; Pelliccione, C. J.; Zhang, W.; Wang, J.; Knehr, K. W.; Wang, J.; Wang, F.; West, A. C.; Marschilok, A. C.; Takeuchi, K. J.; Takeuchi, E. S. Dispersion of Nanocrystalline Fe3O4 within Composite Electrodes: Insights on Battery-Related Electrochemistry. *ACS Appl. Mater. Interfaces* **2016**, *8* (18), 11418−11430.
(132) Bock, D. C.; Waller, G. H.; Mansour, A. N.; Marschilok, A. C.; Takeuchi, K. J.; Takeuchi, E. S. Investigation of Solid Electrolyte Interphase Layer Formation and Electrochemical Reversibility of Magnetite, Fe3O4, Electrodes: A Combined X-ray Absorption Spectroscopy and X-ray Photoelectron Spectroscopy Study. *J. Phys. Chem. C* **2018**, *122* (26), 14257−14271.
(133) Wu, H.; Jia, H.; Wang, C.; Zhang, J. G.; Xu, W. Recent Progress in Understanding Solid Electrolyte Interphase on Lithium Metal Anodes. *Adv. Energy Mater.* **2021**, *11* (5), 2003092.
(134) Sungjemmenla; S K, V.; Soni, C. B.; Kumar, V.; Seh, Z. W. Understanding the Cathode-Electrolyte Interphase in Lithium-Ion Batteries. *Energy Technology* **2022**, *10* (9), 2200421.
(135) Bruck, A. M.; Brady, N. W.; Lininger, C. N.; Bock, D. C.; Brady, A. B.; Tallman, K. R.; Quilty, C. D.; Takeuchi, K. J.; Takeuchi, E. S.; West, A. C.; Marschilok, A. C. Temporally and Spatially Resolved Visualization of Electrochemical Conversion: Monitoring Phase Distribution During Lithiation of Magnetite (Fe3O4) Electrodes. *ACS Applied Energy Materials* **2019**, *2* (4), 2561−2569.
(136) Cui, J.; Zheng, H.; He, K. In Situ TEM Study on Conversion-Type Electrodes for Rechargeable Ion Batteries. *Adv. Mater.* **2021**, *33* (6), No. e2000699.
(137) He, K.; Zhang, S.; Li, J.; Yu, X.; Meng, Q.; Zhu, Y.; Hu, E.; Sun, K.; Yun, H.; Yang, X. Q.; Zhu, Y.; Gan, H.; Mo, Y.; Stach, E. A.; Murray, C. B.; Su, D. Visualizing non-equilibrium lithiation of spinel oxide via in situ transmission electron microscopy. *Nat. Commun.* **2016**, *7*, 11441.
(138) Li, J.; Hwang, S.; Guo, F.; Li, S.; Chen, Z.; Kou, R.; Sun, K.; Sun, C. J.; Gan, H.; Yu, A.; Stach, E. A.; Zhou, H.; Su, D. Phase evolution of conversion-type electrode for lithium ion batteries. *Nat. Commun.* **2019**, *10* (1), 2224.
(139) Li, Q.; Li, H.; Xia, Q.; Hu, Z.; Zhu, Y.; Yan, S.; Ge, C.; Zhang, Q.; Wang, X.; Shang, X.; Fan, S.; Long, Y.; Gu, L.; Miao, G. X.; Yu, G.; Moodera, J. S. Extra storage capacity in transition metal oxide lithium-ion batteries revealed by in situ magnetometry. *Nat. Mater.* **2021**, *20* (1), 76−83.
(140) Hu, Y. Y.; Liu, Z.; Nam, K. W.; Borkiewicz, O. J.; Cheng, J.; Hua, X.; Dunstan, M. T.; Yu, X.; Wiaderek, K. M.; Du, L. S.; Chapman, K. W.; Chupas, P. J.; Yang, X. Q.; Grey, C. P. Origin of additional capacities in metal oxide lithium-ion battery electrodes. *Nat. Mater.* **2013**, *12* (12), 1130−1136.
(141) Laruelle, S.; Grugeon, S.; Poizot, P.; Dollé, M.; Dupont, L.; Tarascon, J.-M. On the Origin of the Extra Electrochemical Capacity Displayed by MO/Li Cells at Low Potential. *J. Electrochem. Soc.* **2002**, *149*, A627.

https://doi.org/10.1021/acs.chemmater.4c02013
Chem. Mater. 2024, 36, 9299−9319